Hydration State and Updip Fluid Migration in the Slab Mantle

Nestor G. Cerpa, Ikuko Wada

JGR Solid Earth

RESEARCH ARTICLE
10.1029/2024JB030609

Hydration State and Updip Fluid Migration in the Slab Mantle

Nestor G. Cerpa[1] **and Ikuko Wada**[2]

[1]Geosciences Montpellier, University of Montpellier, CNRS, University of Antilles, Montpellier, France, [2]Department of Earth and Environmental Sciences, University of Minnesota, Minneapolis, MN, USA

Key Points:

- Dehydration in the subducting mantle can lead to updip fluid migration along the dehydration front within the slab mantle
- Updip fluid migration in the slab mantle is more likely for younger (<~30 Ma) slabs because of the smaller required hydration thickness
- Fluids produced in the slab mantle at sub-arc to post-arc depths are redirected toward the sub-forearc through updip migration

Supporting Information:

Supporting Information may be found in the online version of this article.

Correspondence to:

N. G. Cerpa,
nestor.cerpa@umontpellier.fr

Citation:

Cerpa, N. G., & Wada, I. (2025). Hydration state and updip fluid migration in the slab mantle. *Journal of Geophysical Research: Solid Earth*, *130*, e2024JB030609. https://doi.org/10.1029/2024JB030609

Received 24 OCT 2024
Accepted 14 JUN 2025

Author Contributions:

Conceptualization: Nestor G. Cerpa
Data curation: Nestor G. Cerpa, Ikuko Wada
Formal analysis: Nestor G. Cerpa, Ikuko Wada
Investigation: Nestor G. Cerpa
Methodology: Nestor G. Cerpa
Validation: Nestor G. Cerpa, Ikuko Wada
Visualization: Nestor G. Cerpa, Ikuko Wada
Writing – original draft: Nestor G. Cerpa, Ikuko Wada
Writing – review & editing: Nestor G. Cerpa, Ikuko Wada

Abstract Fluid production from dehydration reactions and fluid migration in the subducting slab impact various subduction processes, including intraslab and megathrust earthquakes, episodic slip and tremor, mantle wedge metasomatism, and arc-magma genesis. Quantifying those processes requires a good knowledge of the location and amount of fluid release from the slab and eventual outflux at the top of the slab. Compaction-pressure gradients induced by the dehydration reactions could drive fluid flow in the slab, even in the updip direction, but how the initial hydration in the oceanic mantle prior to subduction impacts the fluid flow has not been investigated. Here, we use a 2-D two-phase flow model to investigate this effect under various initial slab-mantle hydration states and slab thermal conditions, both of which impact the depth extent of the stability of hydrous minerals. We focus on the lateral shift between the site of dehydration reactions and the location of fluid outflux at the top of the slab due to intraslab-updip migration. Our results indicate that major updip fluid pathways form along the antigorite and chlorite dehydration fronts sub-parallel to the slab surface. This, in turn, promotes fluid outflux at the slab surface as shallow as 30–40 km depths. This mechanism is more likely in young slabs (<~30 Ma) as its warm condition results in a relatively thin (<~20-km thick) stability zones of hydrous phases in the incoming oceanic mantle, which leads to the formation of the slab-parallel dehydration fronts and updip fluid migration.

Plain Language Summary Subduction zones are where a relatively dense oceanic tectonic plate thrusts under another tectonic plate. There, potentially devastating geological processes, such as earthquakes and volcanism, occur. Many of these processes are strongly impacted by the migration and distribution of fluids within and above the subducting plate. However, the mechanisms governing fluid migration and distribution at depths remain poorly understood. In this study, we conduct numerical simulations of fluid migration within a slowly deforming (i.e., creeping at geological timescales) subducting plate that is hydrated prior to subduction and releases fluids as it experiences increasing temperature and pressure with depth. We explore various pre-subduction hydration and thermal conditions of the subducting plate, both of which influence the amount of fluid release at depths. Our numerical simulations show that fluids that are released at relatively large depths (e.g., ~100 km depth) can travel within the subducting slab toward shallower depths against the direction of subduction over tens of kilometers away from their source. This significantly impacts the overall distribution of fluids and thus geological processes at shallower depths. We propose that this updip migration is more prevalent in subducting slabs that are less than about 30 million years in age.

1. Introduction

Water (aqueous fluids) plays a critical role in many subduction zone processes, such as arc magma generation, slow and fast earthquakes, and chemical cycles. Water is transported into subduction systems as pore fluids in the subducting sediments and crust that are generally expelled at relatively shallow depths (<~20 km depth) (Hyndman & Peacock, 2003). Water is also transported as mineralogically bound water in hydrous minerals, such as lawsonite, antigorite, chlorite, and talc. The stability of these hydrous minerals is controlled by pressure and temperature, and thus their dehydration and breakdown occurs over depth ranges that are unique to the specific spatio-temporal evolution of the pressure-temperature (PT) conditions of the subducting material (e.g., Hacker et al., 2003; K. Okamoto & Maruyama, 1999; Schmidt & Poli, 1998; Ulmer & Trommsdorff, 1995). The dehydration may affect the physical properties of the rocks, such as density and frictional strength. The released fluids may further affect mechanical state of the rock by elevating pore fluid pressure at the site of dehydration, potentially triggering earthquakes through the hypothesized mechanism of dehydration embrittlement (Kirby et al., 1991; Yamasaki & Seno, 2003) or stress transfer to the surrounding material (Ferrand

et al., 2017). Fluid migration away from the site of the dehydration reactions controls the fluid flux at the subduction interface and therefore fluid availability for other processes, such as seismic and aseismic sliding along the subduction interface (Audet et al., 2009; Condit et al., 2020; Hyndman et al., 2015; Kodaira et al., 2004; Saffer & Tobin, 2011) and hydrous melting of the subducting crust and sediments and the overriding mantle wedge (Bouilhol et al., 2015; Grove et al., 2006). This study focuses on the spatial relations between the locations of dehydration and the subsequent migration and distribution of fluids in the subducting material, including the distribution of fluid outflux at the top of the subducting slab (hereafter referred to as the ToS outflux).

The distribution of ToS outflux has previously been quantified, using thermo-petrologic models for fluid source calculations, commonly assuming instantaneous upward fluid migration within the slab (Cerpa et al., 2022; Hacker, 2008; Rupke, 2004; Van Keken et al., 2011; Wada et al., 2012). Other models that assume buoyancy-driven porous flow in the subducting slab predicts sub-vertical fluid migration in the slab (i.e., relatively small lateral transport, which is caused by the motion of the slab) (Hebert et al., 2009; Iwamori, 1998). However, models that additionally incorporate the effect of compaction pressure predict significant updip fluid flow within the subducting slab (Morishige & Van Keken, 2018; Wilson et al., 2014). This occurs as fluid production via dehydration creates porosity, which is volumetrically balanced by the (de)compaction of the porous matrix. The gradients of compaction pressure, in addition to fluid buoyancy, in turn, drive fluid migration.

Observations, such as high Vp/Vs ratios in the subducting oceanic crust in northern Cascadia at 25–45 km depths (Peacock et al., 2011), experimental evidence of porosity in natural metamorphic rock samples at pressures equivalent to <~90-km depth (Ganzhorn et al., 2019), and geological records of vugs in Monviso-Alps eclogite (Angiboust & Raimondo, 2022), all point to the presence of a fluid-filled porosity of up to a few vol% or wt.% in metamorphic rocks down to at least 50–90 km depth. Moreover, based on observations from exhumed rocks in fossil subduction systems, several pathways for fluids in the subducting material have been proposed, including pathways through a layer of highly sheared or mechanically mixed material along the subduction interface (Muñoz-Montecinos et al., 2021; Piccoli et al., 2021; Tulley et al., 2022) and within the subducting crust and the top-most subducting mantle (Angiboust et al., 2014; Huber et al., 2022; John et al., 2012).

Since fluid migration is thought to be impacted by the distribution of fluid sources as they generate compaction pressure gradients, dehydration of subducted material may provide a pathway for updip fluid migration within the slab. In particular, the pre-subduction hydration of the incoming oceanic mantle near the trench plays an important role in setting up the distribution of fluid sources and thus fluid production at depths (Cerpa et al., 2022; Van Keken et al., 2011). However, constraining the degree and extent of hydration in the incoming oceanic mantle remains challenging. Here, we refer to the slab-normal thickness of the stability zones of hydrous minerals in the slab mantle as the stability thickness and the slab-normal thickness of the hydrated slab mantle as the hydration thickness. The stability thickness in the oceanic mantle is thermally limited and is small (~several kilometers) for very young oceanic plates, such as the Juan de Fuca plate in Cascadia (Horning et al., 2016). However, as geochemical analyses of arc magma in Cascadia indicate contribution of fluids from the slab mantle (e.g., Walowski et al., 2015), the oceanic mantle can be hydrated even in very young oceanic plate. For older and colder oceanic plates, the stability thickness is greater, but the hydration thickness may be limited more by the fluid availability. Further, the hydration of the oceanic mantle may occur along deep-cutting normal faults near the trench, as observed in a number of subduction zones, such as off Nankai (Arnulf et al., 2022), Nicaragua (Miller et al., 2021; Naif et al., 2015; Ranero et al., 2003), Chile (Ivandic et al., 2010; Van Avendonk et al., 2011), and NE Japan (Obana et al., 2019), and the hydration may be highly heterogeneous, potentially impacting the fluid migration pathways in the slab. In this study, we investigate the effects of the stability and hydration thickness, water content, and localization of hydration in the incoming oceanic mantle on fluid migration, using two-dimensional two-phase fluid flow models. In the models, fluid sources are incorporated based on the pre-computed pseudosections of water content for crustal and mantle lithologies. We focus on relatively young subducting slabs (ages up to 30 Ma), for which we find that updip flow within the slab from the sub-arc to forearc depths is most efficient, influencing the mechanical coupling along the plate interface, forearc mantle wedge hydration, and sub-arc mantle melting.

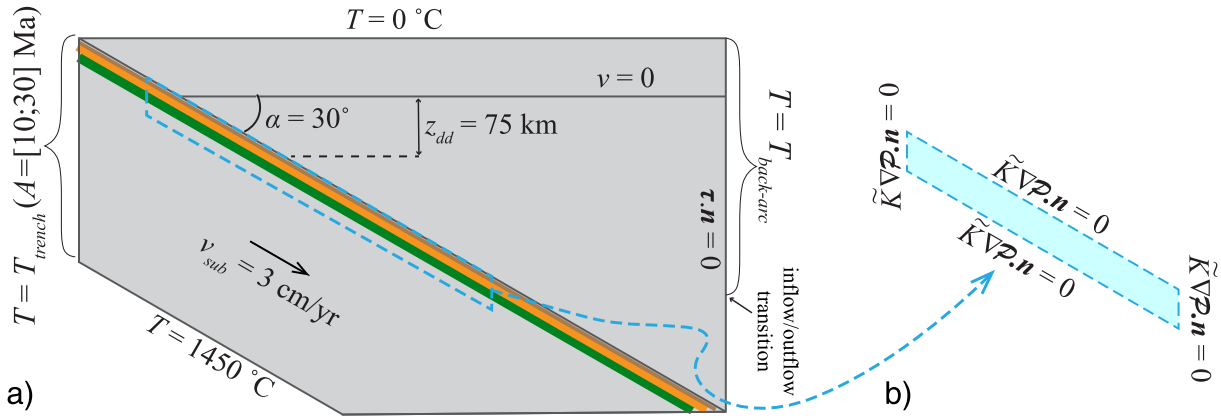

Figure 1. Sketch of computational domains for (a) solid-state mantle flow and (b) intraslab fluid flow, including the boundary conditions in dimensional units. The three colors in panel (a) illustrate the three layers assumed in our lithological model: basaltic crust (brown), gabbroic crust (orange), and hydrated lithospheric mantle (green).

2. Methods

In our two-phase flow models, the solid-state mantle wedge flow is first calculated and is independent of the fluid flow under the small-porosity assumption (Katz et al., 2007; Spiegelman, 1993) and the simplification that fluids do not affect solid rheology.

The governing equations for the solid-state mantle wedge flow are those of the incompressible Stokes equation, and the heat equation is solved everywhere in the computational domain (Figure 1a; Text S1 in Supporting Information S1) (Cerpa et al., 2017; Lee et al., 2021; Van Keken et al., 2002; Wada et al., 2008). We assume wet olivine dislocation creep as the main deformation mechanism in the mantle wedge. The dimensional shear viscosity is expressed as:

$$\frac{1}{\eta} = \frac{1}{\eta_{\text{disl}}} + \frac{1}{\eta_{\text{max}}}$$

where η_{max} is a dimensional maximum viscosity and η_{disl} is given by:

$$\eta_{\text{disl}} = A C_{\text{OH}}^{\beta} \exp\left(\frac{E}{RT}\right)^{-1/\gamma} \dot{\varepsilon}_{II}^{\left(\frac{1-\gamma}{\gamma}\right)}$$

with a pre-exponential factor $A = 3.0 \times 10^{-20}$ Pa$^{-\gamma}$ s^{-1}, the water content $C_{\text{OH}} = 1{,}000$ H/10^6 Si, the activation energy $E = 4.80 \times 10^5$ J mol^{-1}, the gas constant $R = 8.3145$, and the water content and the stress exponents $\beta = 1.2$ and $\gamma = 3.5$, respectively (Hirth & Kohlstedt, 2003).

Since the sensitivity of the mantle wedge flow to model parameters is not the focus here, we use the maximum slab-mantle decoupling depth (MDD) of 75 km (Wada & Wang, 2009), a subducting plate velocity of 3 cm/yr, and a slab dip of 30° in all models. Similarly, we neglect radiogenic heat sources and shear heating when solving the heat equation. The velocity boundary conditions for the calculation of the mantle wedge flow field are indicated in Figure 1. The temperature condition on the trench-side vertical boundary of the model is calculated by using the GDH1 plate cooling model (Stein & Stein, 1992), assuming a plate age of 10, 20 or 30 Ma. On the shallow part ($\lesssim$35 km depth) of the back-arc-side vertical boundary, we impose a geotherm calculated by a one-dimensional conductive model that neglects internal heat production, and on the deeper part down to approximately the mantle inflow-outflow transition depth, we impose a geotherm calculated by a potential temperature of 1450°C and an adiabatic gradient of 0.3°C km^{-1}. The top and the bottom boundaries have a constant temperature of 0°C and 1450°C, respectively. These boundary conditions do not evolve with time.

To estimate the amount of fluid release by dehydration reactions within the slab, we assume full thermodynamic equilibrium and adopt a relatively simple lithological model, which consists of three layers: a 2-km thick basaltic crust with 3.1 wt.% initial water content, a 5-km thick gabbroic crust with 0.8 wt.% initial water content, and a

partially serpentinized mantle layer, for which we consider thicknesses of 6, 12, and 22 km, and initial water contents of 2 wt.% (~15% serpentinization) or 6.5 wt.% (~50% serpentinization). The degree of serpentinization of the subducting mantle is difficult to constrain, and varying degrees of serpentinization among and within subduction zones have been reported based on P-wave speeds measured at the outer-rise (Cerpa et al., 2022; Grevemeyer et al., 2018; Zhang et al., 2024). Given the uncertainties, we choose a relatively low and high values of water content of 2 wt.% and 6.5 wt.%, which correspond roughly to 15% and 50% of serpentinization, to illustrate its impact on the fluid migration pattern. Unless otherwise stated, we assume uniform hydration (i.e., spatially uniform water content) in each lithologic layer. We compute pseudo-sections of water content using the thermodynamic code Perple_X (Connolly, 2009) and thermodynamic database of Holland and Powell (2011). The bulk composition assumed for the basaltic and gabbroic crustal layers are taken from Hacker (2008), except that we account for a one-layer basaltic crust by extending their upper-volcanic up. For the hydrated peridotite we use the bulk composition used in Cerpa et al. (2022). The details of the bulk compositions that we assume in our study are in Table S1 in Supporting Information S1. The solid solutions used for thermodynamic calculations with Perple_X are those given in Cerpa et al. (2022).

The governing equations of fluid flow are as described in Cerpa et al. (2017, 2018) except that the effects of variations in grain size and fluid viscosity are excluded and that a source term (rate of mass transfer from solid to fluid) is incorporated to account for the effect of fluid release due to dehydration reactions within the subducting slab (Text S1 in Supporting Information S1) (Wilson et al., 2014). In the model, fluid flow is driven by density contrast between the fluid and the solid phase and compaction pressure gradients, and the effect of tectonic pressure gradients is not included. We solve non-dimensionalized equations with the scaling parameters listed in Table S2 in Supporting Information S1. In particular, unless otherwise stated, we use a reference permeability of 10^{-7} m^2, which corresponds roughly to the permeability with a mean grain size of 5 mm based on the empirical law of Wark et al. (2003). This reference permeability leads to a reference fluid-to-solid velocity ratio of approximately 40, which is similar to the "moderate fluid mobility" case of Wilson et al. (2014). We use a reference shear viscosity of 10^{20} Pa s for the subducting slab in our models, unless otherwise stated. The average shear viscosity of the subducting slab is not well constrained. Dynamic subduction models suggest it may be at least 100 times that of the average shear viscosity of the upper mantle (Ribe, 2010; Schellart, 2008) and thus potentially in the order of 10^{22}–10^{24} Pa s. However, several mechanisms that may partially weaken the subducting slab have been proposed, including bending-related weakening (Gerya et al., 2021; Rose & Korenaga, 2011). The apparent lowering of shear viscosity in our model is to take the effect of these weakening mechanisms into account. We nonetheless test the sensitivity of our models to the choice of the reference permeability and reference shear viscosity on fluid migration patterns in Section 3.6.

The fluid flow equations are solved only for a select section of the slab domain that is relevant to the depths of slab dehydration (Figure 1b). The depth extent of the computation domain increases with the thermal age of the slab to capture major dehydration reactions in the subducting slab mantle. In solving the fluid flow equations, non-zero and non-negative porosity values are enforced to keep the porosity physically meaningful. Although enforcing a positive porosity has been shown to produce some errors in fluid-mass conservation, resulting in a slight overestimation of fluid flux, its impact on the overall fluid migration patterns is relatively small (Lee et al., 2024).

Note that, although our models are computed with non-dimensionnalized equations, all results below will be given in dimensional units for simplicity.

3. Results

3.1. Solid-State Mantle Flow Models and Fluid Sources

We first compute the solid-state mantle flow and the thermal structure for two slab ages: 10 and 30 Ma (Figures 2a and 2b, respectively). Using the results and the pseudo-sections for the basaltic crust, the gabbroic crust and the hydrated mantle, we compute the rate of mass (water) transfer from solid to fluid, hereafter also referred to as the fluid source, within the slab sub-domain. In the two models, we use the initial bulk water content of 2.0 wt.% and full hydration thickness (i.e., hydration over the largest stability thickness, which is approximately 10 and 20 km for the 10- and 30-Ma slabs, respectively) in the slab mantle.

The dehydration within the basaltic crust occurs approximately between 500 and 600°C in both the 10- and 30-Ma slabs (Figure 2), owing to the breakdown of minerals such as chlorite, lawsonite, and talc (Figure 3a). Small

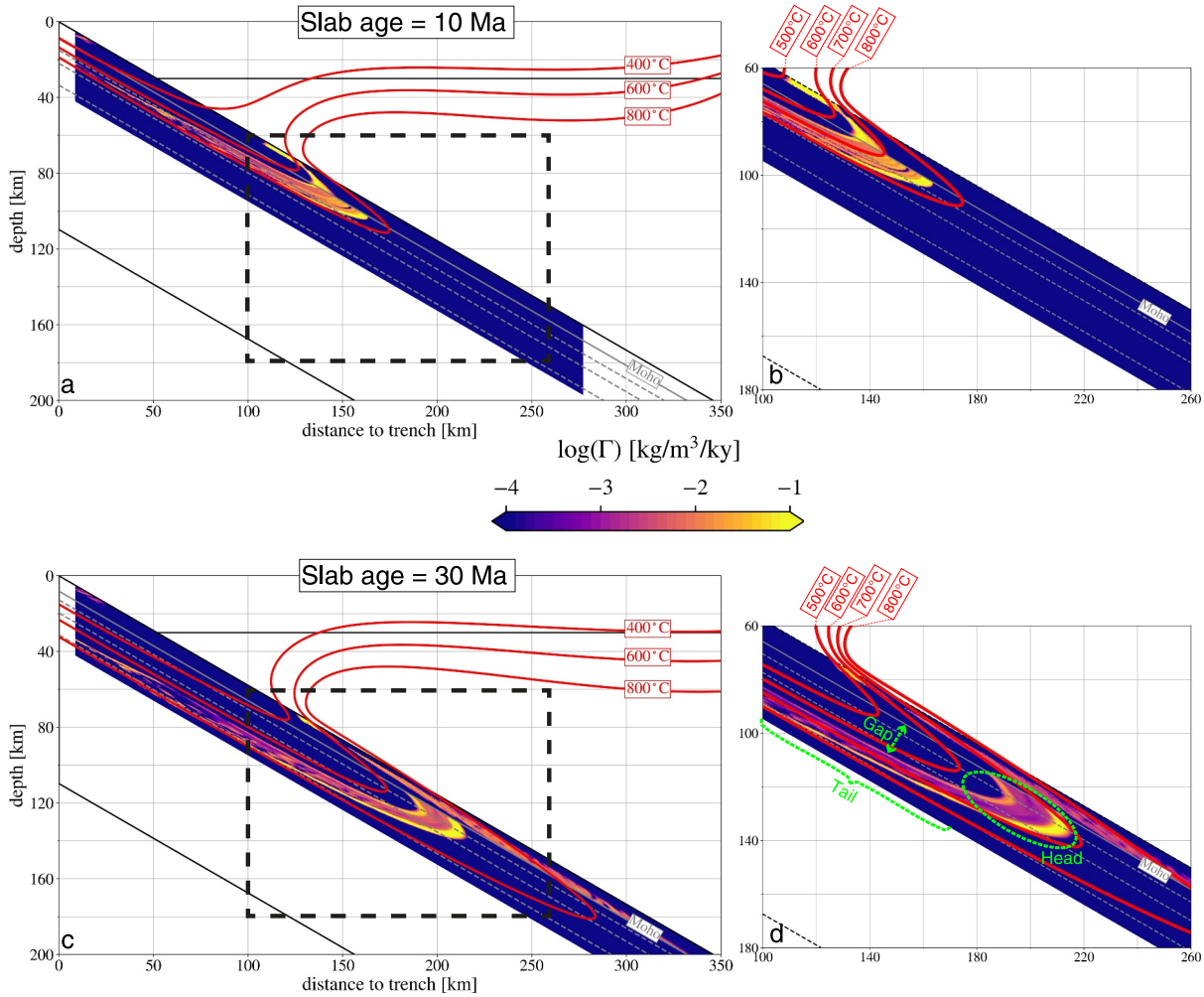

Figure 2. Temperature contours (red lines) and fluid source Γ (color scale) predicted in the 10-Ma slab (a, b) and in the 30-Ma slab models (c, d). Right panels show the sub-region illustrated by a dashed rectangle in the left panels. The updip and downdip outermost bounds of the fluid source region in the slab mantle are defined largely by the antigorite-out and chlorite-out reactions, respectively (Figure 3). We refer to these boundaries of the slab-mantle fluid source region as the antigorite and chlorite dehydration fronts, respectively. The thin gray lines indicate the slab Moho. The gray dashed lines indicate possible mantle hydration thicknesses of 6, 12, and 22 km.

differences in the dehydration depths are observed between the two models, as those temperatures are reached at 60–70 km depths at the slab top in the 10-Ma slab and 70–75 km depths at the slab top in the 30-Ma slab. Since, shear heating along the subduction interface is neglected in our models, the dehydration depths may be slightly overpredicted (e.g., Van Keken et al., 2018).

The depth of dehydration of the gabbroic crust displays more variation between the two slabs. In the 10-Ma slab, the dehydration of the gabbroic layer occurs over a narrow temperature range of 650–700°C and at depths shallower than ~95 km (Figure 2b). Conversely, in the 30-Ma slab, this dehydration front is much more spread out, taking place mostly between 700 and 850°C, spanning the depth range of approximately 95–180 km.

In the slab mantle, two main dehydration reactions occur in both 10-Ma and 30-Ma slabs: the breakdown of antigorite followed by the breakdown of chlorite (Figure 3b). Below pressures of ~5 GPa, the negative Clapeyron slope of the antigorite-out reaction is much steeper than that of the chlorite-out reaction, making the latter more sensitive to temperature. As a result, these reactions near the slab Moho occur approximately at 650°C and 750°C, respectively, in the 10-Ma slab (red line in Figure 3b) whereas they occur at 650°C and 700°C, respectively, in the 30-Ma slab (magenta line in Figure 3b). The corresponding depth extent of these reactions varies with the distance to the Moho. Within the top 6 km of the slab mantle, the breakdown of both hydrous minerals takes place between 85 and 100-km depths in the 10-Ma slab, and between 125 and 140-km depths in the 30-Ma slab (Figures 2 and

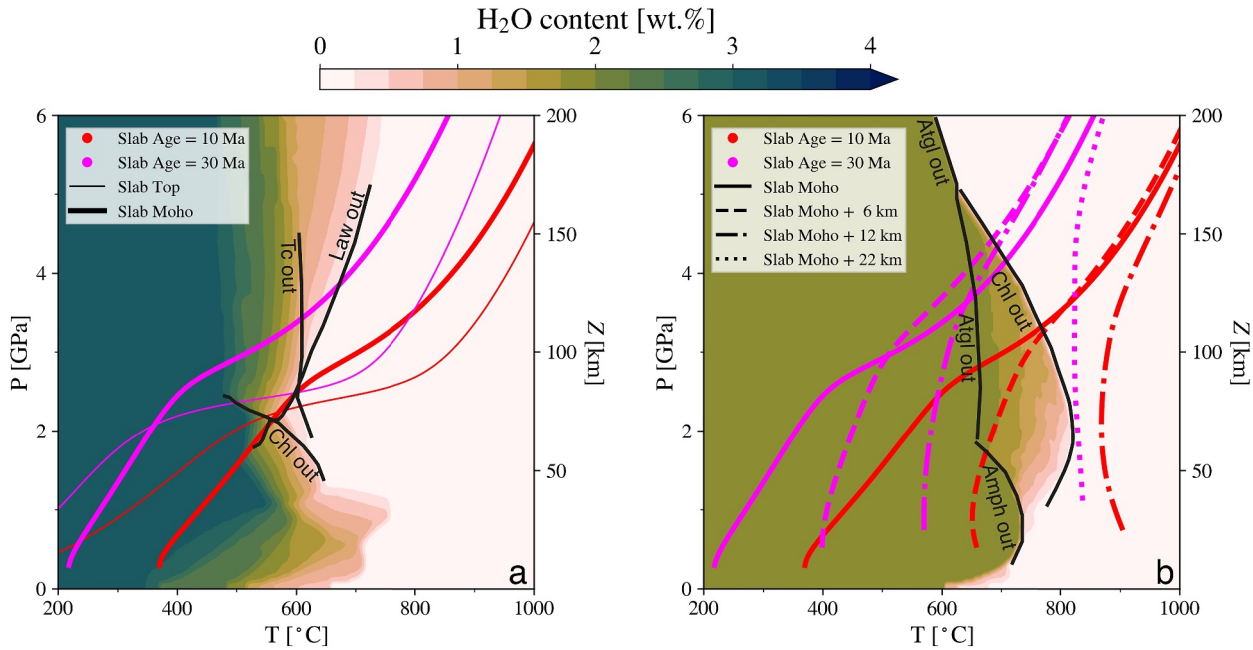

Figure 3. PT conditions along the slab top and several slab-parallel profiles in the 10-Ma slab (red lines) and 30-Ma slab (magenta lines) plotted on top of diagrams of bound-water content (wt.%) for (a) the basaltic crust and (b) the hydrated peridotitic mantle. The bound-water content was calculated by using Perple_X (Connolly, 2009). The PT profiles are along the slab top (thin continuous lines), along the slab Moho (thick continuous lines), and at three different depths below the slab Moho: 6 km (dashed lines), 12 km (dotted-dashed lines), and 22 km (dotted lines). The stability limits of the major hydrous phases are indicated by black lines. For simplicity, in what follows, the dehydration fronts that are associated with hydrous-mineral breakdown reactions, especially antigorite and chlorite break-down reactions, are referred to as the (antigorite and chlorite) dehydration fronts, respectively. Moreover, to refer to the general shape of the fluid sources within the subducting mantle we will describe it in terms of head, tail and gap of the dehydration fronts (see Figure 2d). The head refers to the most downdip part of the antigorite and/or chlorite dehydration fronts that is generally in the top ~10 km below the slab Moho. The tails refer to the dehydration fronts that are sub-parallel to the slab Moho. The gap refers to the slab-normal distance between the slab Moho and the tail of the antigorite dehydration front.

3b). Note that with increasing temperature, the maximum water content of the mantle rock decreases, resulting in progressive fluid production. At higher perpendicular distance below the slab Moho, the breakdown reaction of antigorite and chlorite are sub-parallel to the slab top and can occur as shallow as 30 to 40-km depths (Figure 3b). That is because of the negative Clapeyron slope of the breakdown reactions, especially for the chlorite-out reaction, leading to a reaction found at lower pressure with increasing temperature.

The fluid production computed in the solid-state mantle flow models are used as a fluid source in the fluid flow models described below. Although the fluid source in the slab mantle is computed over the full stability thickness, we apply cutoff thicknesses of 6, 12, and 22 km (dashed gray lines on Figure 2) in the fluid flow model to evaluate the effect of the hydration thickness in the incoming oceanic plate.

We work under the assumption of uniform hydration of the incoming plate unless stated otherwise. For the assumed steady-state subduction zone thermal structure and with a constant subduction rate, the spatial distribution of fluid sources does not vary with time. Thus, below, we refer to these sources as either static fluid sources or simply as fluid sources.

3.2. Reference Fluid Flow Model

We refer to the fluid flow model for the 10-Ma slab with the hydration thickness of 6 km and the initial mantle water content of 2 wt.% as the reference fluid flow model (Figures 4 and 5a). The model is run for a dimensional time of 9 My.

Initially ($t \leq 0.2$ My, Figure 4a), the porosity builds up at the locations of fluid production. Fluid migration mostly occurs near the dehydration front within the crust. The fluid flow relative to the moving solid matrix, hereafter referred to as the separation velocity, is driven by density contrast between the fluid and the solid phase and compaction pressure gradients as defined in the governing equations. The fluid buoyancy results in upward fluid

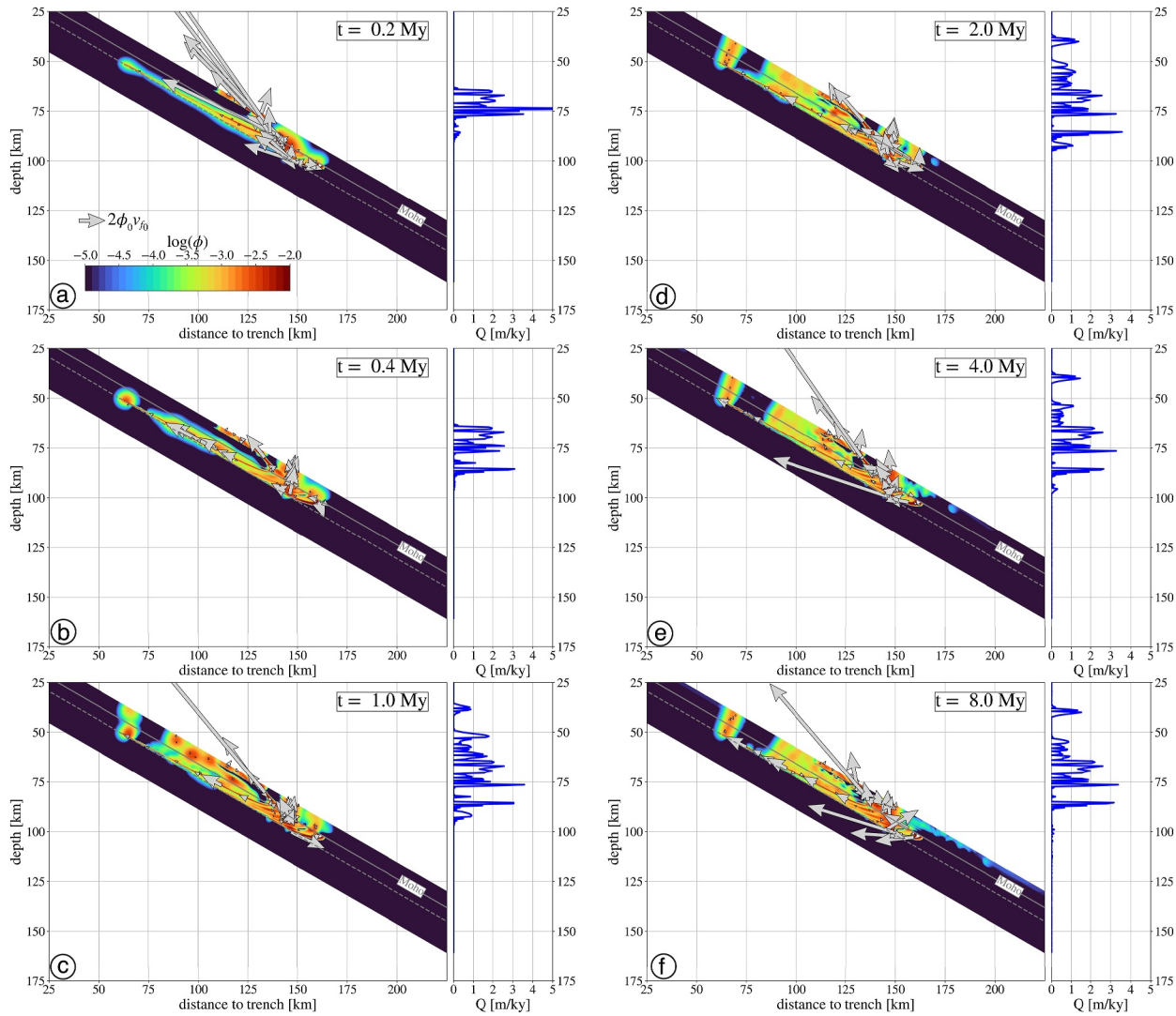

Figure 4. Time snapshots (a–f) of the evolution of the porosity field ϕ (color), the separation velocity $\phi(\vec{v_f} - \vec{v_s})$ (vectors) within the slab subdomain, and that of the ToS outflux Q in the reference fluid flow model for the 10-Ma slab with the hydration thickness of 6 km and the mantle initial water content of 2 wt.%. The solid and dashed gray lines indicate the Moho and the bottom of the hydrated mantle, respectively. To help legibility, only separation velocities with magnitudes of $0.1 \times \phi_0 v_{f_0}$ or greater are displayed.

migration. Yet, the main migration path develops sub-parallel to the dehydration front in the crust. These fluid pathways are due to compaction pressure gradients that develop along the locations of fluid sources. Within the slab mantle, some of the fluids that are produced in the most downdip parts (>80-km depth) of the 6-km thick hydrated layer migrate upward directly toward the ToS, but the majority of them rather connect to the fluid pathways along the reaction front within the crust. At this stage, the fluids produced within the slab mantle between 50 and 80-km depths hardly segregate from the downgoing solid, owing to a relatively low porosity ($\phi \ll 10^{-3}$) at the tail of the dehydration front that does not generate significant compaction -driven flow. Overall, in this early stage, fluids reach the ToS mostly at 65–75 km depths, peaking at 70–75 km depths, just above the dehydration front in the uppermost basaltic crust.

At a later time of 0.4 My (Figure 4b), some of the fluids produced from the gabbroic crust and the head of the dehydration fronts in the slab mantle migrate upward and start to reach the ToS. This is illustrated by the appearance of a secondary peak in the ToS at around 85-km depth. Furthermore, within the slab mantle, the porosity at the source locations mostly reaches values equal or higher than 10^{-3}, potentially enhancing compaction-driven flow relative to fluid advection by the solid, and thus fluids start to migrate by buoyancy and

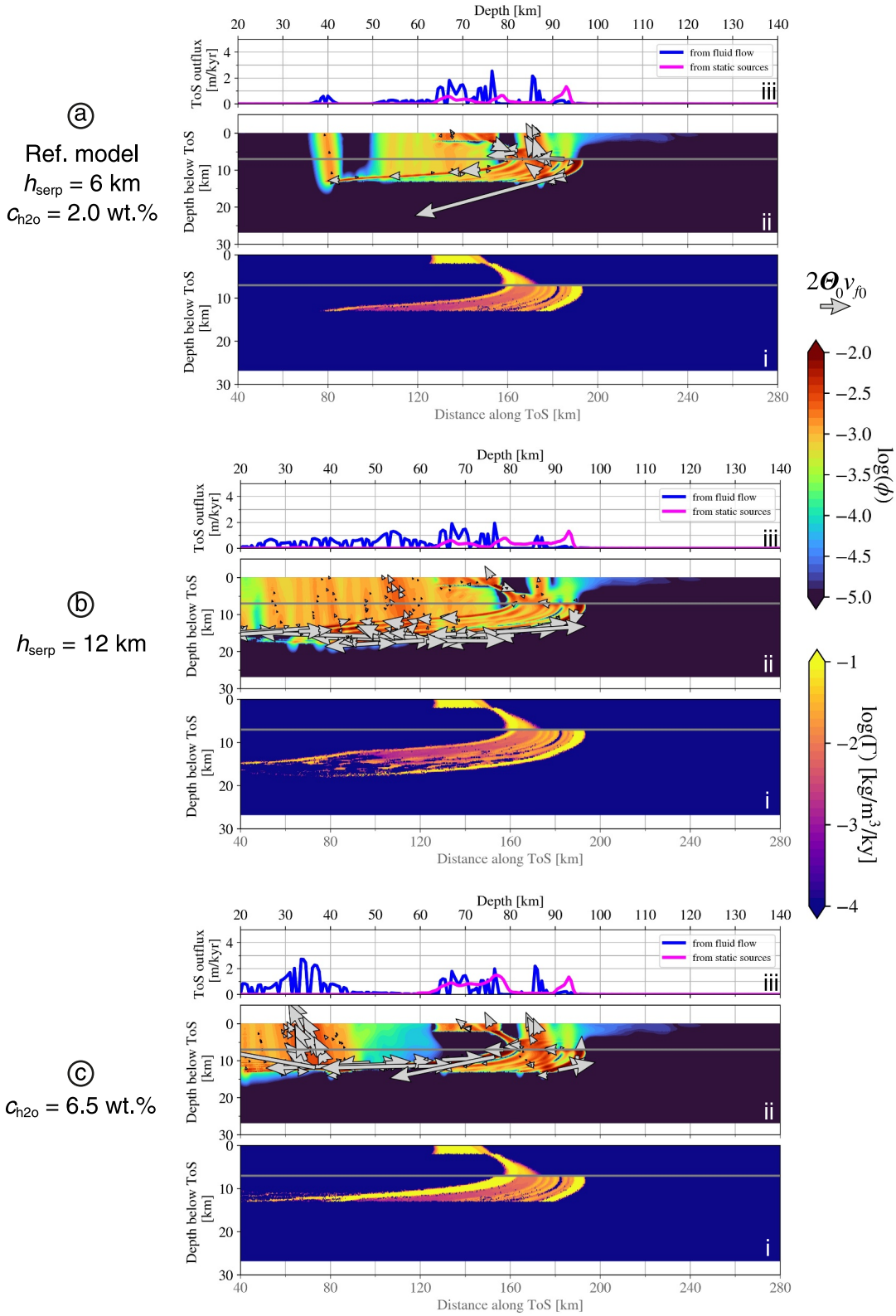

Figure 5.

compaction-driven flow. Fluid migration occurs mostly updip in the form of porosity waves along the antigorite dehydration front, producing another main fluid pathway sub-parallel to the subducting-slab top. Porosity waves are localized and transient increase in porosity that arises from the interaction between fluid segregation and solid deformation under the governing equations of porous flow in a viscous media. In our model, the propagation of these waves is driven by pressure gradients and fluid's buoyancy (Barcilon & Richter, 1986; Scott & Stevenson, 1984; Spiegelman, 1993). For example, propagation of a singular fluid pulse would promote the compaction of the solid matrix ahead of the pulse and decompaction at its trailing edge. Decompaction and compaction of the matrix would, in turn, lead to fluid discharge and recharge, respectively, which would contribute to the motion of the fluid. At the same time, behind the compacted matrix, an area of decompaction would also uptake fluids, leading to the generation of moving waves. It is worth noting that, in our models, although porosity waves are most noticeable at early stages of the models (i.e., before 1 My) and in the most-updip part of the tails of the dehydration fronts, fluid migration occurs as porosity waves everywhere where fluids are present and at any time during the model simulation.

At a time of 1 My, fluids migrating along the tail of the slab-mantle dehydration front eventually start to migrate upwards, mainly driven by buoyancy, crossing overlying regions of the slab mantle, which initially had unseen fluids pass through (Figure 4c). These updip and then upward migration pathways to the ToS result in new peaks in the ToS outflux at 30–70-km depths. In particular one peak at 35–40-km depths is due to the upward migration of fluids that accumulate at the updip end of the antigorite dehydration front.

At more evolved times (t = 1–8 My), despite the strong time-dependence of fluid migration, the long-term main fluid pathways appear. One of the main pathways connects the head (>80-km depth) of the dehydration front in the slab mantle to the head of dehydration front in the gabbroic crust, and finally to the dehydration front in the basaltic crust (Figures 4d–4f). Another main pathway runs from the same downdip part of the mantle dehydration front to the ToS as a result of buoyancy-driven flow. Finally, the other main pathway brings slab-mantle fluids updip along the antigorite dehydration front and then to ToS due to buoyancy-driven flow, providing the shallowest ToS outflux (∼40-km depth).

To better assess the long-term fluid pathways and distribution relative to the fluid source, we compute the time-averaged porosity and separation velocity fields for the reference fluid flow model between 2 and 9 My (see Figure 5a(ii)). The time-averaged distributions are similar to those at 8 My (Figure 4f). The updip fluid migration along the antigorite dehydration front in the slab mantle leads to fluid migration in regions that lack fluid sources between 40 and 80-km depths. The distribution of time-averaged ToS outflux (blue line on Figure 5a(iii)) is also similar to the ToS outflux at 8 My, featuring three main peaks at depths of 65–70, ∼75, and ∼85 km. Finally, a secondary peak is at ∼40-km depth and illustrates the updip fluid migration path along the antigorite dehydration front. This ToS outflux distribution is in contrast to the distribution based on the assumption of instantaneous vertical fluid migration from the fluid sources (magenta line on Figure 5a(iii)). The latter, which we referred to as the static ToS outflux distribution, has only three peaks. They are of less magnitude but are wider compared to the ones computed from the fluid flow model described above. The peaks in the static distribution occur at 65–75, ∼80, and 90–95 km depths and are downdip compared to the major peaks predicted by the fluid flow model.

3.3. Effects of Thickness and Degree of Hydration in the Incoming Plate

We now evaluate how assumptions on the hydration state of the mantle in the incoming oceanic plate affects our results by increasing the hydration thickness to 12 km in one model (Figure 5b) and the initial water content of 6.5 wt.% (Figure 5c), relative to the reference model.

Larger hydration thickness results in the much shallower updip extent (to ∼ 80 km depth) of both the antigorite and the chlorite stability limits in the slab mantle (Figure 5b(i)), leading to greater updip fluid migration than the

Figure 5. Results of fluid flow models assuming a 10-Ma slab with: (a) a 6-km thick serpetinized mantle and an initial water content of 2 wt.% (reference fluid flow model), (b) a 12-km thick serpentinized mantle and an initial water content of 2 wt.%, and (c) a 6-km thick serpentinized mantle and an initial water content of 6.5 wt.%. Each subpanel displays (from bottom to top) (i) the distribution of fluid sources (color), (ii) the time-averaged porosity (color) and separation velocity (gray vectors; to help readability, only separation velocities with magnitudes equal or higher than $0.1 \times \phi_0 v_{f_0}$ are displayed), and (iii) distribution of the model-predicted and static (blue and magenta, respectively) ToS outflux. The model-predicted ToS outflux is the time-average fluid flux across the slab-top boundary (i.e., $\phi v_f \cdot n$ where n is the boundary-normal unit vector). The static ToS outflux is based on the vertical integration of the fluid sources, assuming vertical instantaneous fluid migration, as indicated in Figure 4 for the 10-Ma slab.

reference model, as illustrated by the higher magnitude of separation velocity along the dehydration fronts (Figure 5b(ii)). The higher amounts of fluid migrating updip within the mantle also lead to more prominent upward migration from the tail of the antigorite dehydration front toward the ToS. The pattern of the ToS outflux has similarities to that of the reference model in that it has three peaks at depths of 65–70, 75, and 85 km. The shallowest two are mainly controlled by the main fluid pathways that develop along the tail of the dehydration front in the slab mantle and in the dehydrating crust. The deepest peak at ∼85-km depth is sourced from the most downdip part of the chlorite dehydration front, but it has a smaller magnitude compared to that in the reference model because some of the fluids flow updip along the chlorite dehydration front in the thicker slab mantle unlike in the reference model. However, the most important difference from the reference model is the nearly continuous ToS outflux between 20 and 65 km depths, with a peak at approximately 55 km, indicating significant updip transport of deeply sourced slab-mantle fluids.

The model with a higher initial water content of 6.5 wt.% in the slab mantle results in a ToS outflux distribution at >65 km depths that is nearly identical to that of the reference model, featuring three major peaks, despite the higher water content. This is because the higher water content leads to a great modal proportion of antigorite while the modal proportion of chlorite is limited by the availability of its key element aluminum, which is relatively low in peridotite (a few wt.% Al_2O_3 in terms of major oxide composition) (Pawley, 2003) and is therefore identical to the reference model. This results in greater fluid production at the antigorite dehydration front compared to the reference model. This results in the fluid production at the chlorite dehydration front that is identical to the reference model. On the other hand, there is greater fluid production at the antigorite dehydration front compared to the reference model, but the fluids migrate updip along the antigorite dehydration front and then upward near the intersection of the antigorite dehydration front and the bottom of the serpentinized slab mantle (i.e., 4 km below the slab Moho), resulting in a broad ToS outflux peak at 30–40 km depths.

3.4. Effects of Slab Age

Given that the depth extent of the dehydration reactions is highly temperature-dependent (Section 3.1), the behavior of updip fluid migration along reaction fronts can vary with the thermal state of the subducting slab. Hence, we explore fluid flow models based on fluid sources that are computed for slab ages of 20 and 30-Ma instead of 10 Ma in the reference model. For those models, we assume hydration thicknesses of 12 and 22 km.

In the 20-Ma slab model, the dehydration reactions occur at greater depths compared to that in the reference 10-Ma slab model (Figure 6a(i)). Within the crust the difference is minor (less than 10 km) for the basaltic layer. The differences are more pronounced in the gabbroic crust where dehydration reactions span 80–130 km depths in the 20-Ma slab, while they occur at 75–85-km depths in the reference 10-Ma slab. Note that the widened reaction front within the gabbroic crust also leads to diminished fluid production within this layer at a given depth (see Figure 6a). As a consequence, the local porosity associated with the fluid production in the 20-Ma slab is relatively low, and thus fluids are more prone to be advected by the subducting slab, as illustrated by the time-average porosity field within the crust (Figure 6a(ii)). The dehydration of the slab mantle near the Moho is deepened by 15–20 km compared to that in the reference 10-Ma slab and occurs at 95–115-km depths. Because the tails of the antigorite and chlorite dehydration fronts in the slab mantle are more than 6 km below the slab Moho, a 6-km hydration thickness as in the reference model would limit the fluid sources in the slab mantle to depths greater than ∼90 km (results not shown). However, a 12-km hydration thickness leads to the updip extension of the trailing part of the antigorite dehydration front, resulting in updip fluid flow and moderate ToS outflux at relatively shallow depths (<70-km depth) (Figure 6a(ii)), similar to the model with a 10-Ma slab with a 6-km hydration thickness.

In the 30-Ma slab case, the depth range of dehydration fronts within the gabbroic crust increases further, spanning 90 km at the top of the gabbroic layer to more than 160 km near the slab Moho. The dehydration reactions in the slab mantle occur at approximately 110-km and 130-km depths near the slab Moho, and in the top 10-km of the mantle, both chlorite and antigorite remain stable beyond 100-km depth. The gap between the slab Moho and the tail of the antigorite dehydration front is much thicker, and a 10-km hydration thickness does not lead to updip flow within the slab mantle, resulting in little ToS outflux at depths shallower than ∼75-km (Figure 6b). However, a hydration thickness of 22 km leads to updip fluid flow within the slab mantle, with a significantly focused flow along the chlorite dehydration front (Figure 6c). In this model, considerable ToS outflux is observed almost continuously between 20 and 75-km depths.

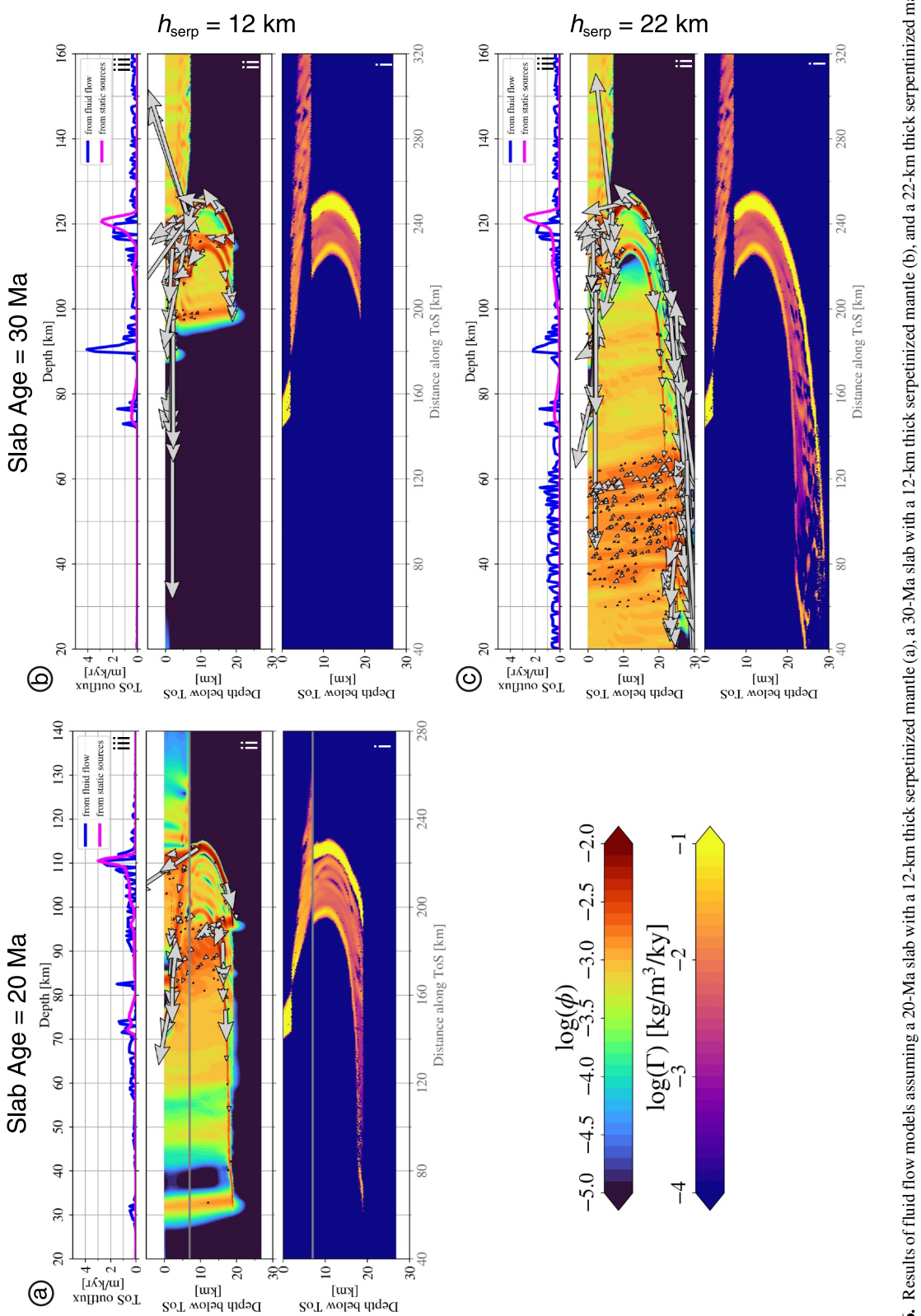

Figure 6. Results of fluid flow models assuming a 20-Ma slab with a 12-km thick serpetinized mantle (a), a 30-Ma slab with a 12-km thick serpetinized mantle (b), and a 22-km thick serpentinized mantle (c). Legend details of all sub-panels are as are as in Figure 5.

3.5. Effects of Localized Fluid Source

Here we test the dependence of the model-predicted fluid flow on the assumption of lateral uniform hydration of the slab mantle (Figure 7). For this, we build an additional fluid flow model with a localized fluid source in the slab mantle. The approximates the potential role of deep-cutting outer-rise normal faults in guiding the fluid percolation and hydration of the oceanic mantle prior to subduction. Note that actual faults are not implemented in our models, and in particular, we do not account for their potential anisotropic hydrological properties (i.e., anisotropic permeability). Instead, we only focus here on the effect of accounting for a localized fluid source, keeping all other model parameters the same.

Localization of fluid sources is implemented by applying a periodic unit-Gaussian function of the horizontal distance to the fluid source distribution that is calculated for uniform hydration with 6.5 wt.% initial water content and hydration thickness of 6 km to represent the lateral variation in the distribution of fluid sources in the slab mantle. The Gaussian function has a peak value of unity, a standard deviation of ∼1 km, and a periodicity of 10 km, assuming hydration along deep cutting normal faults that extend to 6 km below the slab Moho and are spaced at 10 km horizontal distance. In the model, the fluid sources move laterally at the speed of the horizontal component of the subduction velocity (i.e., ∼3.5 cm/yr). With the assumed local hydration, the average water content in the incoming oceanic slab mantle works out to be 0.6 wt.%. This is about a third of what is assumed for the reference model with the uniform hydrated slab mantle of 2 wt.%.

At the very early stages of the fluid flow model (t = 0.1 My), non-zero porosity values in the slab mantle are observed only around the vertical columns with fluid sources that approximates the hydration along faults (Figure 7a), resulting in the development of transient vertical localized fluid flow paths. The porosity field within the crust is similar to that in the reference fluid flow model. As time progresses to t = 0.2 My, the laterally moving fluid sources create porosity all the way along the motion and the regions with non-zero porosity widen and become interconnected. The ToS outflux distribution shows only one major broad peak at depths of roughly 65–80 km, reflecting the release of fluids originating from the basaltic and the gabbroic crust. Eventually at t = 0.4 My, despite the localized sources, the porosity created by the sources become interconnected, and the model displays a fluid distribution similar to the model with the assumption of a uniform hydration (i.e., that in the reference fluid flow model). Also, by this time, the fluids produced at the deepest parts of the antigorite and chlorite dehydration fronts are able to reach the surface, and a second major peak in the ToS outflux appears at depths of approximately 90–100 km. At later times of the model, updip fluid migration occurs along the antigorite dehydration front, similar to the reference fluid flow model. As a consequence, relatively uniform ToS outflux appears between 30 and 65 km depths.

The time-averaged porosity field illustrates the observations at the mature stages of the model where updip flow occurs along the antigorite dehydration front. Compared to the reference model with uniform hydration (Figure 5a), the ToS outflux at depths shallower than the MDD becomes less localized (e.g., the lack of the secondary peak at 40 km depth that is described for the reference model) and is more uniformly distributed.

3.6. Role of the Reference Permeability and the Mantle Bulk Viscosity

We further test the sensitivity of our models to the choice of the two important scaling parameters for fluid flow: the reference permeability and reference shear viscosity. All other fluid flow parameters remain as in the reference fluid flow model.

A lower reference permeability by one order of magnitude ($K_0 = 10^{-9}$ m^2, Figure 8a) yields a reference fluid-to-velocity ratio of approximately 10 (similar to the low-fluid mobility case of Wilson et al. (2014)). The lower reference permeability leads to less efficient fluid flow than in the reference fluid flow model. As a consequence, the time-average porosity is higher because fluids injected into the system are not expelled as easily than in the reference model. More importantly, the compaction-driven flow is inhibited, and updip fluid migration barely occurs. Hence, the general pattern of fluid outflux at the ToS resembles that of the static sources. In particular, the ToS outflux at depths shallower than the MDD becomes negligible.

A higher reference permeability by one order of magnitude ($K_0 = 10^{-6}$ m^2, Figure 8b) yields a reference fluid-to-velocity ratio of approximately 180 (similar to the high-fluid mobility case of Wilson et al. (2014)). The higher reference permeability leads to a more efficient fluid flow than in the reference model, resulting in a time-average porosity that is lower than in the reference model. Compaction-driven flow becomes dominant, particularly

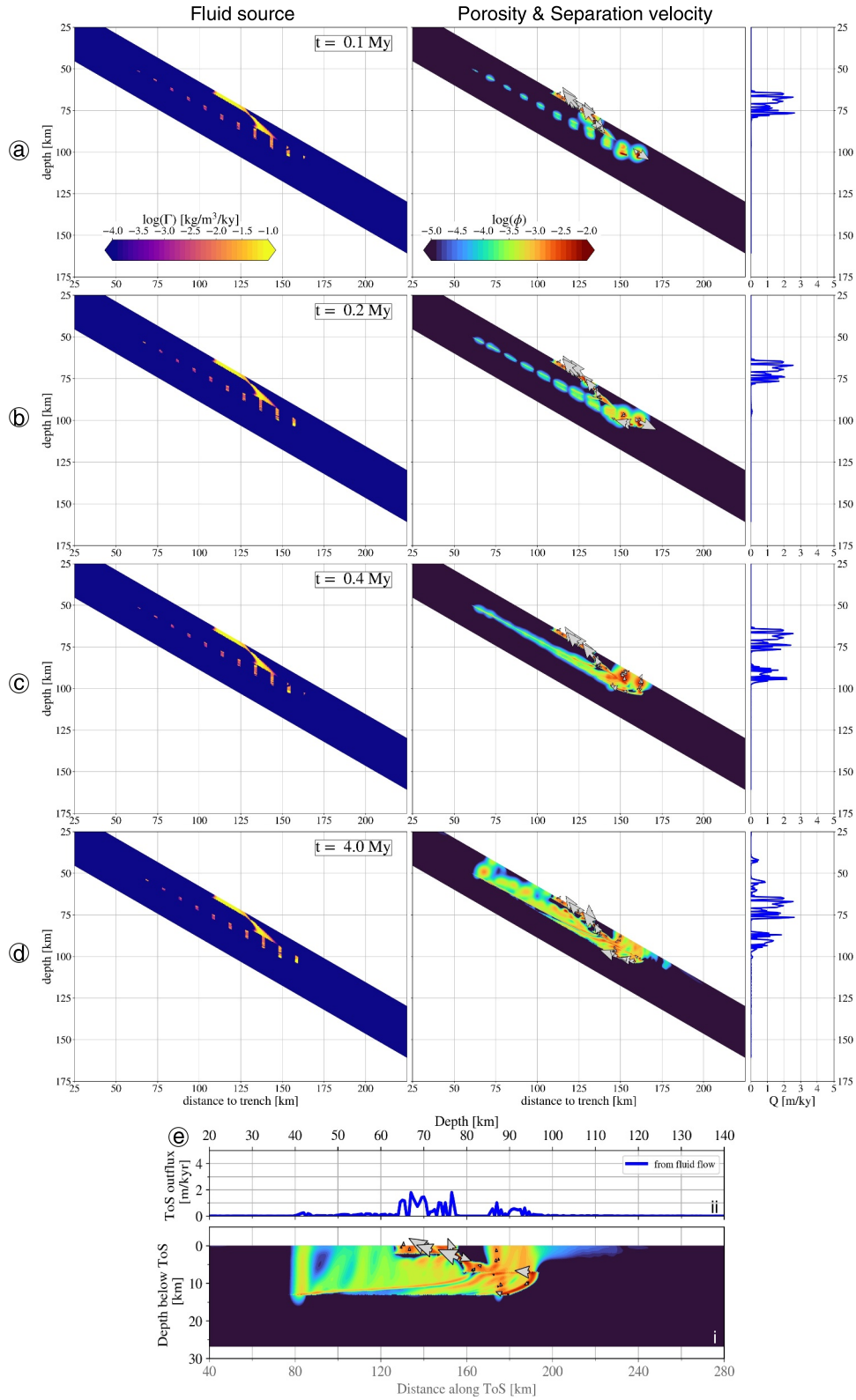

Figure 7. Time-snapshots (a–d) and time-average (e) of modeling results considering a laterally heterogeneous hydration of the slab mantle along faults. Legend details are as in Figures 4 and 5.

10.1029/2024JB030609

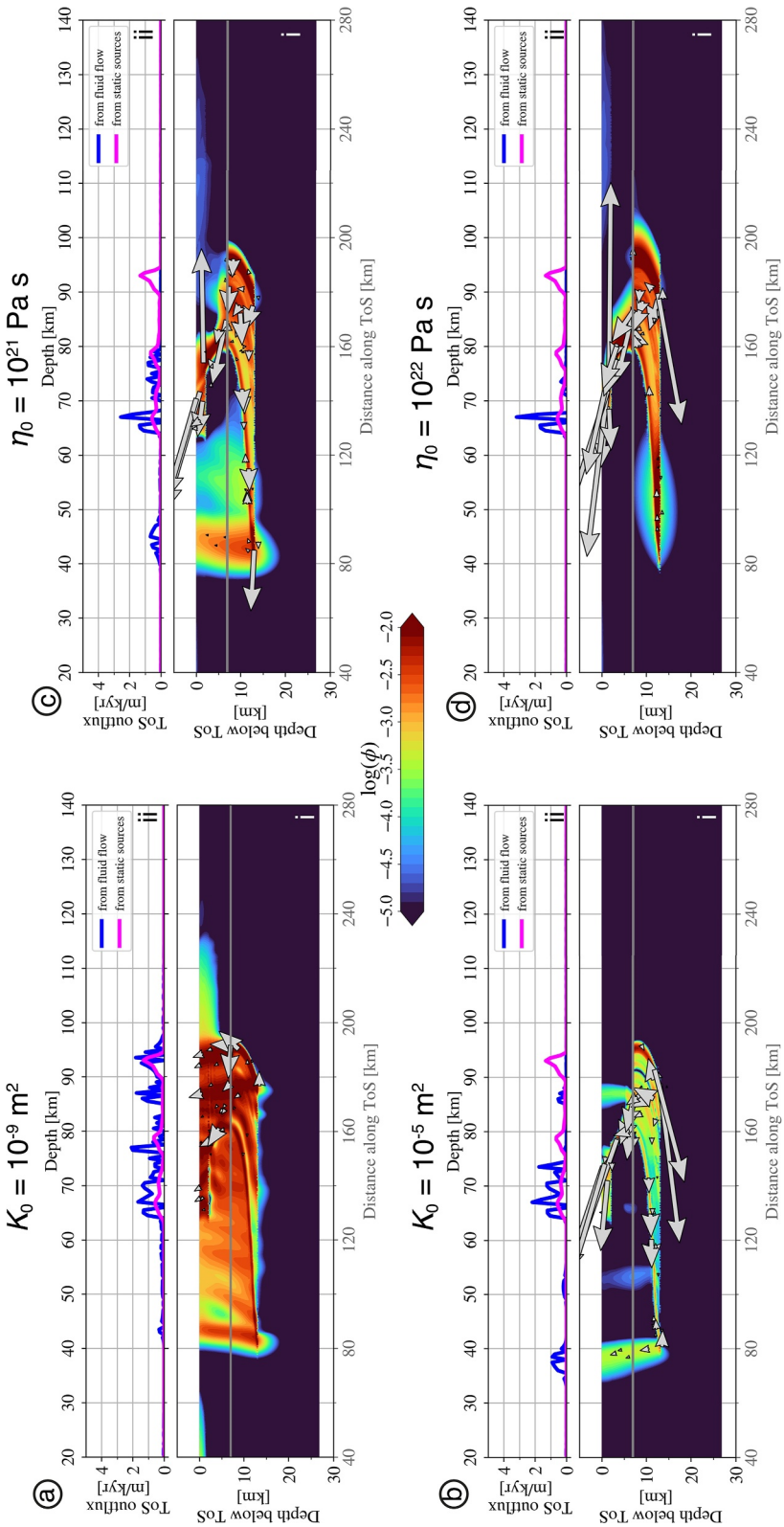

Figure 8. Model results with variable reference permeability K_0 (left) and shear viscosity η_0 (right) relative to the reference fluid flow model. Legend details are as in Figure 5. Note that the final time for the models with $\eta_0 = 10^{21}$ Pa s and $\eta_0 = 10^{22}$ Pa s is 12, and 15 My, respectively.

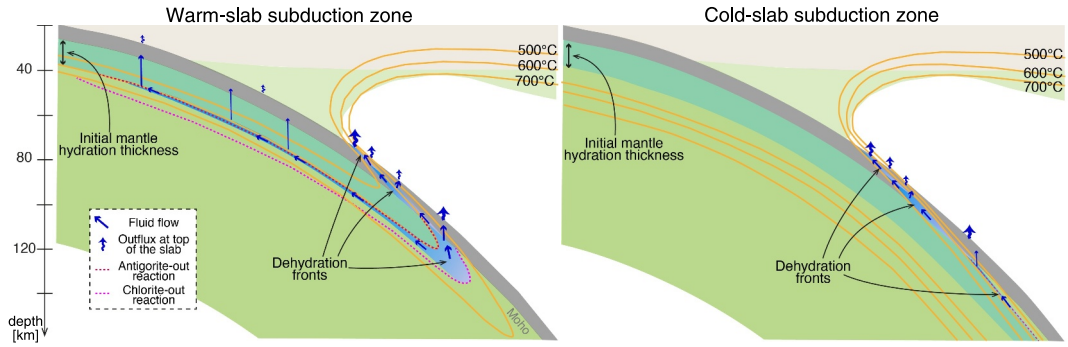

Figure 9. Graphical summary of (a) the main results of our study focusing on warm-slab subduction zones in comparison to (b) the cold-slab subduction zone, as predicted by Wilson et al. (2014). Note that the isotherms in panels (a) and (b) approximately follow those of subduction zones with a 20-Ma slab and a 50-Ma slab, respectively. For simplicity, we assume the same initial mantle hydration thickness in both cases.

leading to a preferential fluid flow along the dehydration reactions, thus updip migration. The fluids originating from the sources in the slab mantle either migrate along the reaction fronts in the mantle or connect to the fluid sources within the crust. At the ToS, the fluid-outflux peak at approximately 85-km depth observed in the reference model is absent in this model with a higher permeability. This is because in the reference model this peak is mainly due to buoyancy-driven flow of fluids originating from the head of the dehydration front in the slab mantle. Hence, fluid outflux at the ToS shows one major peak between 65 and 75-km depths and a minor peak between 35 and 40 km.

A higher reference shear viscosity by one order of magnitude ($\eta_0 = 10^{21}$ Pa s) leads to a higher reference bulk viscosity $\zeta_0 = \eta_0 \phi_0^{-1}$, thus a higher resistance of the porous media to compaction (Figure 8c). The higher resistance to compaction generates a much slower fluid motion and thus the time-average porosity shows higher magnitudes than the reference model. However, the higher resistance to compaction inhibits the vertical fluid flow more than the updip flow. Although it occurs at a much lower rate than in the reference model, the updip fluid migration still leads to a small peak of ToS outflux at approximately 45-km depth. A further increase in the reference shear viscosity eventually leads to inhibition of fluid migration, especially updip migration in the slab mantle (Figure 8d).

4. Discussion

4.1. Comparison to Previous Modeling Studies of Instraslab Fluid Flow

Our fluid flow models are similar to those of Wilson et al. (2014), who first demonstrated the potential of updip fluid migration along fluid sources in the subducting slab due to compaction-driven flow (Figure 9). In their model, the subducting slab was 50-Ma, older than our modeled cases, and the hydrated part of the subducting mantle was 2-km thick. Given the older slab age and the relatively small hydration thickness in their model, only the head of the antigorite dehydration front were present in the slab mantle at ∼160-km depth, and the tail of the dehydration front was absent. As a consequence, the updip fluid migration in the slab mantle was limited to the depths corresponding to the heads of the antigorite dehydration front (Figure 9b). Instead, significant updip fluid migration occurred within the crust, primarily along the dehydration front within the gabbroic crust over 150–300-km depths beneath the arc. Thus, this updip fluid migration did not result in redistribution of ToS outflux to depths shallower than the MDD, as observed in our models with warmer slabs. Our results indicate that such redistribution of the ToS outflux for older (>30 Ma) slabs can only occur if the hydration thickness in the slab mantle exceeds potentially unrealistic values of 20–30 km (Figure 9a).

Morishige and Van Keken (2018) also developed fluid flow models for the subducting slab, using viscoelastic rheology and incorporating the effect of compaction. In their model, a fluid source region was placed arbitrarily in the slab as a dipping thin segment that is a few kilometers in thickness and extends over ∼20 km in horizontal distance. They showed that a bulk viscosity of 10^{21} Pa s favored upward gravity-driven migration while higher bulk viscosities permitted updip migration within the fluid source region. In particular, they showed that a viscosity of 10^{26} Pa s, which placed their models close to the elastic regime, also allowed updip migration. Note that

they use values of permeabilities at reference porosities that are higher ($K(\phi_0) \in [10^{-11}; 10^{-15}]$ m^2) than those at our equivalent reference porosities ($K(\phi_0) = K_0\phi_0^3 \sim 10^{-15}$ m^2). This may explain why their model predicted updip fluid migration even with bulk viscosities as high as 10^{24}–10^{26} Pa s.

Larger-scale dynamic models of subduction show the unbending of the subducting slab leads to pressure gradients due to tectonic stresses that may affect the migration of fluids along the subduction interface and in the slab (Angiboust et al., 2012; Babeyko & Sobolev, 2008; Dorbath et al., 2008; Faccenda et al., 2012). Faccenda et al. (2012) predicted that in the unbending region of the slab, tectonic overpressure develops in the vicinity of the slab Moho while under-pressure develops in the cold core of the slab further away from the slab top. Consequently, they suggested that the resulting pressure gradients drive the fluids liberated near the Moho to migrate toward the core of the slab. Furthermore, once the fluids reach the region of under-pressure in the core, the fluids migrate updip along a plane of neutral slab-normal tectonic pressure gradients. This is an additional mechanism for updip fluid migration in the slab mantle that is not taken into account in our models. In addition, Angiboust et al. (2012) suggest that weak regions and strain localization develop below and atop the oceanic crust due to fluid circulation, and may promote updip fluid flow, if a strain-dependent permeability is active. Although compaction was absent in the models of Faccenda et al. (2012) and Angiboust et al. (2012), we hypothesize that these mechanisms work together with the effect of compaction to boost the updip fluid migration. The degree of the combined effect likely depends on the thermal age and hydration thickness of the incoming oceanic plate.

4.2. Potential Impact of Model Assumptions

The lithologic model that is assumed for the subducting material in our study does not include a sediment layer, and the basaltic crust is characterized by one composition although the composition (e.g., water content) likely varies with depth within the basaltic layer (Hacker, 2008). Although these simplifications in the model are unlikely to impact the updip flow in the slab mantle, they impact the distribution of the fluid sources in the uppermost part of the subducting slab, thereby potentially creating additional pathways for updip migration. For example, in warm-slab subduction settings, metapelites have been reported to dehydrate slightly deeper and more continuously than average MORB compositions (Condit et al., 2020). However, the dehydration pattern of a sediment layer can vary significantly with its composition (e.g., pelagic vs. terrigeneous; Hacker, 2008), and it is beyond the scope of this study to quantify the effect of the sediment layer on the overall intra-slab flow pattern. Despite these uncertainties, for a given slab age, the depth ranges of dehydration of the metasedimentary layer and the basaltic crust are expected to be relatively narrow compared to that of the slab mantle, especially when the pre-subduction hydration thickness is larger than ~5–10 km. Therefore, the effect of variations in the composition on the depth distribution of the fluid source and resulting updip fluid transport in the uppermost part of the slab are likely small relative to the effect of the updip transport within the slab mantle over the possible ranges of stability thickness (slab's thermal state) and hydration thickness.

In the calculations of fluid sources, we used the phase assemblages in the slab crust and mantle predicted by equilibrium-thermodynamics approaches. However, experimental petrology on complex systems predicts the stability of other hydrous phases, including the 10-Å or Mg-Sursassite phases, beyond the stability temperature of antigorite and chlorite and at pressures 3–7 GPa (Fumagalli et al., 2001; Gies et al., 2024; Hermann & Lakey, 2021; Maurice et al., 2018). The dehydration of these phases would shift the head of the major dehydration front in the slab mantle further downdip and increase the gap between the slab Moho and the tail of the dehydration front (e.g., Cerpa et al., 2022). The impact of these hydrous phases on the depths of dehydration in the slab mantle would be greatest if the temperature condition of the hydrated slab mantle falls in the temperature range of 600–800°C at 4–5 GPa. For the relatively young slabs (<30 Ma), however, the temperature condition in the slab mantle is generally higher than 800°C at 4–5 GPa, and therefore the impact of these hydrous phases on the updip migration in the slab mantle would be small (Figure 3b).

In our study, although we tested the impacts of the reference permeability and solid viscosity, we assumed spatially uniform values for these parameters. Cerpa et al. (2017) showed that the spatial variation in the grain size (permeability) and viscosity impacted the prediction of fluid pathways in the ductile mantle wedge corner in two-phase flow models. Likewise, in the subducting slab, the various lithologies may yield different hydraulical and rheological properties and may thus impact intraslab fluid migration (Ganzhorn et al., 2019; Hirth et al., 2001; Hirth & Kohlstedt, 2003; Tielke et al., 2017; Zhang & Green, 2007). Furthermore, anisotropic permeability along the foliation of the sheared subduction interface may also contribute to updip flow atop of the subducting slab

(Angiboust et al., 2012; Kawano et al., 2011; Lee & Kim, 2023). Field studies have indeed reported evidences of updip channelized flow within the sheared subduction interface (Bebout & Penniston-Dorland, 2016; Breeding et al., 2004; Taetz et al., 2018) and at the contact between the subducting oceanic crust and mantle (Angiboust et al., 2014; Piccoli et al., 2021). These additional mechanisms of updip fluid migration should not affect the migration within the slab mantle that we highlight in our model. However, the overall budget of updip fluid migration that incorporates the effects of the rheological and hydraulical changes across subducting-lithological boundaries should be quantified in future studies.

In our model, we neglect the reaction of the migrating fluids with the surrounding rocks, which has been suggested to impact the fluid outflux at the ToS and the predictions of chemical fluxes at this boundary (Malvoisin et al., 2015; Tian, Katz, & Rees Jones, 2019; Wada et al., 2012; Zhong & Galvez, 2022). For instance, the infiltration of aqueous fluids originating from the slab mantle could result in further hydration of the updip and overlying material above the tail of the slab-mantle dehydration fronts that are not fully hydrated. Based on the predictions by Wada et al. (2012), we speculate that such an uptake of the migrating fluids would delay and shift the ToS outflux peaks downdip. However, this effect is likely temporary until the material along the fluid migration pathways become fully hydrated. Furthermore, the infiltration of H_2O-rich fluids originating from the dehydration of the slab mantle into the overlying oceanic crust may also cause a series of re-equilibration reactions between the fluid and the rock, modulating the onset temperature of devolatilization as the CO_2-content re-equilibrates, thus impacting the overall depth of devolatilization (Tian, Katz, Rees Jones, et al., 2019). Our models show that fluids liberated near the head of the dehydration fronts in the slab mantle could be preferentially pumped updip, possibly causing the re-equilibration effect to occur within the slab crust at shallower depths than previously predicted.

In this study, the model assumes a Kozeny-Carman type relationship between permeability and fluid fraction, which takes the form of a power law $K = K_0\phi^n$ and approximates grain-scale permeability (i.e., how fluids are arranged at the microstructure scale) for diffuse porous flow. In particular, we assume that, under a textural equilibrium hypothesis, the reference permeability K_0 scales with the square of the grain size (Rudge, 2018; Von Bargen & Waff, 1986; Wark & Watson, 1998), and thus a mean grain size of 5 mm, yields a reference permeability value of 10^{-7} m^2. For porosity values of 10^{-3}–10^{-2}, the permeability in our models is in the order of 10^{-16}–10^{-13} m^2. These permeability values are higher than laboratory and field-derived estimates of permeability of metamorphic rocks in subduction zones, which are more commonly lower than 10^{-18} m^2 (Angiboust & Raimondo, 2022; Ganzhorn et al., 2019; Kawano et al., 2011). However, the higher permeability values in our models are required to allow fluid migration and represent an effective permeability, which also include the effect of fluids in cracks and veins at micro-scale (e.g., Muñoz-Montecinos & Behr, 2023).

In our model, the effect of solid volume change is neglected. Dehydration results in a decrease in solid volume but a net increase in total volume due to fluid production, potentially causing hydrofracturing (e.g., Nishiyama, 1989). Even if the released fluids migrate away faster than their production, which leads to a net decrease in the total volume, fracturing may still occur due to strain gradient across the dehydrating and non-dehydrating regions of the rock (e.g., A. Okamoto & Shimizu, 2015). These fractures can increase permeability beyond the effect of increased fluid fraction alone. However, the orientation of the fracture depends on the background differential stress (A. Okamoto et al., 2017) and may not necessarily be parallel to the dehydration front, resulting in a complex networks of fluid migration pathways.

Antigorite breakdown within the subducting mantle has been suggested to be accommodated by micro-scale olivine vein growth and fluid channeling in directions controlled by the local principal-stress (Muñoz-Montecinos et al., 2024; A. Okamoto et al., 2017; Schmalholz et al., 2023) or by the chemical heterogeneity gradients (Plümper et al., 2017). The effective shear viscosity of the slab mantle locally decreases in response to the vein formation (Schmalholz et al., 2023). This may be consistent with the fact that our models require relatively low reference-solid shear viscosities compared to those that are derived from classical temperature-dependent laws. However, because of a uniform reference solid shear viscosity in our model and because we do not account for the potential effect of fluids on the solid viscosity, fluid-assisted shear localization is not possible in our model. Likewise, the potential feedback between small-scale shear localization and fluid pumping in the subducting slab mantle along bands that are parallel to the dip, as suggested by field observations (Muñoz-Montecinos et al., 2024), remains to be quantified by numerical models of two-phase flow. Furthermore, as the occurrence of intraslab earthquakes indicates, brittle deformation may occur in the subducting slab, potentially resulting in additional fault- and fracture-controlled permeability in the slab. The overall fluid migration pattern may be

impacted by larger-scale variation in permeability due to the presence of faults and fractures. Given the high pressure, the permeability that is associated with these structures are expected to be relatively low except during the time of dilation via faulting or fracture formation. Therefore, grain-scale permeability and those associated with small-scale cracks and veins, whose collective effect is represented by the relatively low reference solid shear viscosity and high reference permeability in our model, likely dominate the overall fluid migration pattern during the absence of faulting and fracture formation.

4.3. Implications for Fluid-Related Processes in Subduction Zones

Intraslab fluid flow may affect both mechanical and chemical processes in the slab, along the subduction interface, and in the overriding material as it impacts the fluid distribution in subduction zones. In particular, our study highlights the possibility of updip fluid migration in the slab mantle over tens of kms, leading to a lateral shift in the fluid distribution from the post-to-sub-arc depths to shallower sub-forearc depths. Such lateral fluid pathways have also been suggested by field studies, for example, in Monviso (Angiboust et al., 2014). They have impact on the relative importance of fluids that are released from the slab crust and the slab mantle, which are discussed below. For this discussion, we classify "relatively young" (<30 Ma) slab ages into two age groups, <15 Ma and 15–30 Ma, based on the expected depths of dehydration in the slab crust and their correlations with the observations to be discussed below. In present-day subduction zones, the dehydration in the crust occurs primarily beneath the cold forearc wedge corner for <15 Ma slabs and at deeper depths for 15–30 Ma slabs (e.g., Van Keken et al., 2011; Wada & Wang, 2009).

Thermo-petrologic models predict that the amount of fluids that are released from the subducting slab beneath the forearc mantle wedge is likely insufficient to significantly hydrate the mantle wedge corner except for subduction zones with a very young (<∼15 Ma) and warm subducting slab, such as Cascadia, Nankai, and Mexico (Abers et al., 2017). This is based on the assumption of vertical fluid migration in the subducting slab. In the fluid source calculation in the slab mantle by Abers et al. (2017), a uniform hydration thickness (2 km) and water content (2 wt.%) for the incoming oceanic mantle were used. While the thicker hydration thickness and higher water content would result in greater fluid production in the slab mantle, the fluid supply for serpentinization in the mantle wedge corner is unlikely to change significantly under the assumption of vertical fluid migration as the slab mantle generally dehydrates downdip of the cold mantle wedge corner. However, with the updip fluid migration mechanism, larger hydration thickness leading to the formation of dehydration front tails could substantially increase the ToS outflux beneath the cold mantle wedge corner for relatively young slabs, and significant hydration of the mantle wedge corner may be possible not only for <15 Ma slabs but also for 15–30 Ma slabs (Figures 6a and 6c). This may explain the observations of serpentinization of the mantle wedge corner at, for instance, Costa Rica (Carlson & Miller, 2003; DeShon & Schwartz, 2004), Kyushu (Xia et al., 2008), and south central Chile (Groß et al., 2008).

Provided that the hydration thickness in the incoming oceanic mantle is close to the stability thickness of antigorite, our models show that significant amounts of slab-mantle derived fluids can travel updip and to the subduction interface at depths as shallow as 30–60 km depths (Figures 5b and 6a, 6c). At this depth range, slow slip events, sometimes referred to as deep SSEs, occur in some subduction zones, with or without associated tremors. Formerly detected in Cascadia (Dragert et al., 2001; Rogers & Dragert, 2003) and Nankai (Obara, 2002), they have been observed in an increasing number of subduction zones over the last two decades (e.g., Beroza & Ide, 2011; McLellan & Audet, 2020). The exact mechanism responsible for triggering deep SSEs remains under vigorous debate (Audet et al., 2009; Behr & Bürgmann, 2021; Kirkpatrick et al., 2021; Wang & Bilek, 2014). It is thought, however, that the sites prone to SSEs may be characterized by high pore fluid pressures (Audet et al., 2009; Royer et al., 2015). Condit et al. (2020) carried thermo-petrological modeling work for Cascadia, Nankai, and Mexico, where the subducting slabs are <∼20 Ma, and predicted that fluid production in sediments and altered basaltic crust could occur at depths consistent with those where deep SSEs are observed in those warm-slab subduction zones. Our results suggest that more fluids could be carried to relevant depths for deep SSEs through updip fluid migration in the warm-subducting slabs. Most importantly, we show that this mechanism may be at work in subduction zones with older slabs (20–40 Ma), where deep SSEs are now observed, such as in northern Chile (Klein et al., 2023), Ecuador (Rolandone et al., 2018), and central Alaska (Ohta et al., 2006). The required hydrated thicknesses that we predict to allow updip fluid migration is roughly compatible with the estimated slab-mantle hydration thickness for nearby regions of observed deep SSEs. For instance, past estimations of the hydration of the subducting mantle of the Nazca plate yielded serpentinized thicknesses of ∼20 km

in northern Chile (23°S; (Ranero & Sallarès, 2004). In western Alaska Peninsula (156°W), a 14–18-km thick serpentinized subducting mantle has been suggested (Li et al., 2024). Development of region-specific models would allow to assess the plausibility of this mechanism for the triggering of deep SSEs.

Earthquakes in the subducting slabs in many subduction zones occur in two parallel planes, one belonging to the subducting crust and the other in the subducting mantle (Brudzinski et al., 2007). Faccenda et al. (2012) hypothesized the association of the lower plane in the slab mantle with the fluid migration along the plane of neutral slab-normal pressure gradients that develop due to the unbending of the slab. Similarly, the updip fluid migration along the tails of the dehydration fronts may also contribute to triggering earthquakes in the lower plane in the slab mantle for relatively young plates. However, this mechanism requires hydration deeper in the incoming oceanic mantle than the updip fluid migration driven by unbending-induced pressure gradients.

In subduction zones with relatively young slabs (<30 Ma), the slab crust dehydrates at relatively shallow depth beneath the forearc, and the fluids for flux melting are largely derived from the slab mantle (Wada & Wang, 2009). With the updip fluid migration in the slab mantle and their partial outflux into the cold forearc mantle wedge (i.e., at depths shallower than 70–80 km), the fluid availability for flux melting in the sub-arc mantle and transport of water to deeper mantle may be lower than currently estimated (Hacker et al., 2003; Van Keken et al., 2011). Future studies should be carried to evaluate the impact a lesser availability of fluids in the sub-arc mantle wedge on the extent of mantle-wedge melting.

Finally, arc volcanoes form in a relatively narrow strip parallel to the margin, suggesting focusing of fluids/melts beneath the arc (England et al., 2004; Syracuse & Abers, 2006). Whether the focusing occurs within the subducting slab or above and whether it occurs prior to the melt generation or after are unclear. From our study, we suggest that relatively young subducting slabs can develop tails of dehydration fronts in the mantle, and lead to a ToS outflux distributed over a wider depth range extending into the forearc region. This would require that a focusing mechanism operates within the mantle wedge (Cerpa et al., 2017; Ha et al., 2020) or in the overlying lithosphere (e.g., Andikagumi et al., 2020; Tibaldi, 1992). On the other hand, in slab that develop only the heads of the dehydration fronts, the ToS outflux can be more focused and deeper beneath the back-arc, resulting in substantially different ToS outflux but still requiring some focusing mechanism for redirection of fluids and magmas towards the sub-arc region.

5. Conclusion

Our study demonstrates the feasibility of significant intraslab updip fluid migration within the subducting mantle of relatively young slabs (<~30 Ma), when the hydration thickness of the incoming oceanic mantle at the trench is comparable to the stability thickness (5–20 km) of the main hydrous minerals in the slab mantle (antigorite and chlorite), allowing the development of dehydration front tails that enable updip migration. We show that fluids produced at the head of the antigorite and chlorite dehydration fronts at the sub-arc to post-arc depths, can travel updip over tens of kms along the dehydration tails, owing to compaction-driven flow, and be released at sub-forearc depths. This mechanism is observed in all our simulations with slab ages of up to 30 Ma, except when model parameters, such as a relatively high reference solid shear viscosities 10^{22} Pa s and/or a relatively low reference permeability 10^{-9} m^2 inhibit fluid migration. Moreover, the model indicates that the updip fluid migration mechanism is independent of whether the hydration in the incoming oceanic mantle is uniform or localized along faults. In nature, the updip fluid flow migration within the slab mantle is most likely to occur in those subduction zones with relatively young slabs (<~30 Ma) unless the hydration thickness in the slab mantle can exceed 20 km. The updip fluid migration can impact various subduction zone processes, including the hydration of the cold sub-forearc mantle wedge corner and slow slip along the plate interface. In particular, for 15–30 Ma slabs, the availability of fluids beneath the forearc is significantly greater than the estimates that assume sub-vertical fluid migration in the slab.

Data Availability Statement

All models presented in the study are run using TerraFERMA v1.0 (Wilson et al., 2017), which is freely available at https://github.com/terraferma/terraferma. For Perple_X we used the pre-compiled version v6.9.0 freely available at https://www.perplex.ethz.ch/perplex/ibm_and_mac_archives/. All information to reproduce our

models is described in the Main Text and in Supporting Information S1. The modeling outputs (time-average fields and fluid outflux at the top of the slab) which are described in the manuscript are available in Cerpa (2025).

Acknowledgments
This research was supported by the Tremplin-ERC Grant LEARNING awarded to NC by the I-SITE excellence program at the University of Montpellier and the National Science Foundation Grant EAR-2246804 to IW. The work was realized with the support of the HPC Platform ISDM-Meso, financed by the Occitanie/Pyrénées-Méditerranée Region, Montpellier Mediterranean Metropole and University of Montpellier.

References

Abers, G. A., Van Keken, P. E., & Hacker, B. R. (2017). The cold and relatively dry nature of mantle forearcs in subduction zones. *Nature Geoscience*, *10*(5), 333–337. https://doi.org/10.1038/ngeo2922

Andikagumi, H., Macpherson, C. G., & McCaffrey, K. J. W. (2020). Upper plate stress controls the distribution of Mariana arc volcanoes. *Journal of Geophysical Research: Solid Earth*, *125*(2), e2019JB017391. https://doi.org/10.1029/2019JB017391

Angiboust, S., Pettke, T., De Hoog, J. C. M., Caron, B., & Oncken, O. (2014). Channelized fluid flow and Eclogite-facies Metasomatism along the subduction shear zone. *Journal of Petrology*, *55*(5), 883–916. https://doi.org/10.1093/petrology/egu010

Angiboust, S., & Raimondo, T. (2022). Permeability of subducted oceanic crust revealed by eclogite-facies vugs. *Geology*, *50*(8), 964–968. https://doi.org/10.1130/G50066.1

Angiboust, S., Wolf, S., Burov, E., Agard, P., & Yamato, P. (2012). Effect of fluid circulation on subduction interface tectonic processes: Insights from thermo-mechanical numerical modelling. *Earth and Planetary Science Letters*, *357–358*, 238–248. https://doi.org/10.1016/j.epsl.2012.09.012

Arnulf, A. F., Bassett, D., Harding, A. J., Kodaira, S., Nakanishi, A., & Moore, G. (2022). Upper-plate controls on subduction zone geometry, hydration and earthquake behaviour. *Nature Geoscience*, *15*(2), 143–148. https://doi.org/10.1038/s41561-021-00879-x

Audet, P., Bostock, M. G., Christensen, N. I., & Peacock, S. M. (2009). Seismic evidence for overpressured subducted oceanic crust and megathrust fault sealing. *Nature*, *457*(7225), 76–78. https://doi.org/10.1038/nature07650

Babeyko, A. Y., & Sobolev, S. V. (2008). High-resolution numerical modeling of stress distribution in visco-elasto-plastic subducting slabs. *Lithos*, *103*(1–2), 205–216. https://doi.org/10.1016/j.lithos.2007.09.015

Barcilon, V., & Richter, F. M. (1986). Nonlinear waves in compacting media. *Journal of Fluid Mechanics*, *164*, 429–448. https://doi.org/10.1017/S0022112086002628

Bebout, G. E., & Penniston-Dorland, S. C. (2016). Fluid and mass transfer at subduction interfaces—The field metamorphic record. *Lithos*, *240–243*, 228–258. https://doi.org/10.1016/j.lithos.2015.10.007

Behr, W. M., & Bürgmann, R. (2021). What's down there? The structures, materials and environment of deep-seated slow slip and tremor. *Philosophical Transactions of the Royal Society A: Mathematical, Physical and Engineering Sciences*, *379*(2193), 20200218. https://doi.org/10.1098/rsta.2020.0218

Beroza, G. C., & Ide, S. (2011). Slow earthquakes and nonvolcanic tremor. *Annual Review of Earth and Planetary Sciences*, *39*(1), 271–296. https://doi.org/10.1146/annurev-earth-040809-152531

Bouilhol, P., Magni, V., Van Hunen, J., & Kaislaniemi, L. (2015). A numerical approach to melting in warm subduction zones. *Earth and Planetary Science Letters*, *411*, 37–44. https://doi.org/10.1016/j.epsl.2014.11.043

Breeding, C. M., Ague, J. J., & Bröcker, M. (2004). Fluid–metasedimentary rock interactions in subduction-zone mélange: Implications for the chemical composition of arc magmas. *Geology*, *32*(12), 1041–1044. https://doi.org/10.1130/G20877.1

Brudzinski, M. R., Thurber, C. H., Hacker, B. R., & Engdahl, E. R. (2007). Global prevalence of double Benioff zones. *Science*, *316*(5830), 1472–1474. https://doi.org/10.1126/science.1139204

Carlson, R. L., & Miller, D. J. (2003). Mantle wedge water contents estimated from seismic velocities in partially serpentinized peridotites. *Geophysical Research Letters*, *30*(5). https://doi.org/10.1029/2002GL016600

Cerpa, N. G. (2025). Data for "hydration state and updip fluid migration in the slab mantle" [Dataset]. *Zenodo*. https://doi.org/10.5281/zenodo.15373661

Cerpa, N. G., Arcay, D., & Padrón-Navarta, J. A. (2022). Sea-level stability over geological time owing to limited deep subduction of hydrated mantle. *Nature Geoscience*, *15*(5), 423–428. https://doi.org/10.1038/s41561-022-00924-3

Cerpa, N. G., Wada, I., & Wilson, C. R. (2017). Fluid migration in the mantle wedge: Influence of mineral grain size and mantle compaction. *Journal of Geophysical Research: Solid Earth*, *122*(8), 6247–6268. https://doi.org/10.1002/2017JB014046

Cerpa, N. G., Wada, I., & Wilson, C. R. (2018). Effects of fluid influx, fluid viscosity, and fluid density on fluid migration in the mantle wedge and their implications for hydrous melting. *Geosphere*, *15*(1), 1–23. https://doi.org/10.1130/GES01660.1

Condit, C. B., Guevara, V. E., Delph, J. R., & French, M. E. (2020). Slab dehydration in warm subduction zones at depths of episodic slip and tremor. *Earth and Planetary Science Letters*, *552*, 116601. https://doi.org/10.1016/j.epsl.2020.116601

Connolly, J. A. D. (2009). The geodynamic equation of state: What and how. *Geochemistry, Geophysics, Geosystems*, *10*(10), 2009GC002540. https://doi.org/10.1029/2009GC002540

DeShon, H. R., & Schwartz, S. Y. (2004). Evidence for serpentinization of the forearc mantle wedge along the Nicoya Peninsula, Costa Rica. *Geophysical Research Letters*, *31*(21), L21611. https://doi.org/10.1029/2004GL021179

Dorbath, C., Gerbault, M., Carlier, G., & Guiraud, M. (2008). Double seismic zone of the Nazca plate in northern Chile: High-resolution velocity structure, petrological implications, and thermomechanical modeling. *Geochemistry, Geophysics, Geosystems*, *9*(7), 2008GC002020. https://doi.org/10.1029/2008GC002020

Dragert, H., Wang, K., & James, T. S. (2001). A silent slip event on the deeper Cascadia subduction interface. *Science*, *292*(5521), 1525–1528. https://doi.org/10.1126/science.1060152

England, P., Engdahl, R., & Thatcher, W. (2004). Systematic variation in the depths of slabs beneath arc volcanoes. *Geophysical Journal International*, *156*(2), 377–408. https://doi.org/10.1111/j.1365-246X.2003.02132.x

Faccenda, M., Gerya, T. V., Mancktelow, N. S., & Moresi, L. (2012). Fluid flow during slab unbending and dehydration: Implications for intermediate-depth seismicity, slab weakening and deep water recycling. *Geochemistry, Geophysics, Geosystems*, *13*(1), 2011GC003860. https://doi.org/10.1029/2011GC003860

Ferrand, T. P., Hilairet, N., Incel, S., Deldicque, D., Labrousse, L., Gasc, J., et al. (2017). Dehydration-driven stress transfer triggers intermediate-depth earthquakes. *Nature Communications*, *8*(1), 15247. https://doi.org/10.1038/ncomms15247

Fumagalli, P., Stixrude, L., Poli, S., & Snyder, D. (2001). The 10Aî phase: A high-pressure expandable sheet silicate stable during subduction of hydrated lithosphere. *Earth and Planetary Science Letters*, *186*(2), 125–141. https://doi.org/10.1016/s0012-821x(01)00238-2

Ganzhorn, A. C., Pilorgé, H., & Reynard, B. (2019). Porosity of metamorphic rocks and fluid migration within subduction interfaces. *Earth and Planetary Science Letters*, *522*, 107–117. https://doi.org/10.1016/j.epsl.2019.06.030

Gerya, T. V., Bercovici, D., & Becker, T. W. (2021). Dynamic slab segmentation due to brittle–ductile damage in the outer rise. *Nature*, *599*(7884), 245–250. https://doi.org/10.1038/s41586-021-03937-x

Gies, N. B., Konrad-Schmolke, M., & Hermann, J. (2024). Modeling the global water cycle—The effect of Mg-sursassite and phase a on deep slab dehydration and the global subduction zone water budget. *Geochemistry, Geophysics, Geosystems*, *25*(3), e2024GC011507. https://doi.org/10.1029/2024GC011507

Grevemeyer, I., Ranero, C. R., & Ivandic, M. (2018). Structure of oceanic crust and serpentinization at subduction trenches. *Geosphere*, *14*(2), 395–418. https://doi.org/10.1130/GES01537.1

Grove, T., Chatterjee, N., Parman, S., & Medard, E. (2006). The influence of H_2O on mantle wedge melting. *Earth and Planetary Science Letters*, *249*(1–2), 74–89. https://doi.org/10.1016/j.epsl.2006.06.043

Groß, K., Micksch, U., & TIPTEQ Research Group, S. T. (2008). The reflection seismic survey of project TIPTEQ—The inventory of the Chilean subduction zone at 38.2° S. *Geophysical Journal International*, *172*(2), 565–571. https://doi.org/10.1111/j.1365-246X.2007.03680.x

Ha, G., Montési, L. G. J., & Zhu, W. (2020). Melt focusing along permeability barriers at subduction zones and the location of volcanic arcs. *Geochemistry, Geophysics, Geosystems*, *21*(12), e2020GC009253. https://doi.org/10.1029/2020GC009253

Hacker, B. R. (2008). H_2O subduction beyond arcs. *Geochemistry, Geophysics, Geosystems*, *9*(3), 2007GC001707. https://doi.org/10.1029/2007GC001707

Hacker, B. R., Abers, G. A., & Peacock, S. M. (2003). Subduction factory 1. Theoretical mineralogy, densities, seismic wave speeds, and H_2O contents. *Journal of Geophysical Research*, *108*(B1), 2001JB001127. https://doi.org/10.1029/2001JB001127

Hebert, L. B., Antoshechkina, P., Asimow, P., & Gurnis, M. (2009). Emergence of a low-viscosity channel in subduction zones through the coupling of mantle flow and thermodynamics. *Earth and Planetary Science Letters*, *278*(3–4), 243–256. https://doi.org/10.1016/j.epsl.2008.12.013

Hermann, J., & Lakey, S. (2021). Water transfer to the deep mantle through hydrous, Al-rich silicates in subduction zones. *Geology*, *49*(8), 911–915. https://doi.org/10.1130/G48658.1

Hirth, G., & Kohlstedt, D. (2003). Rheology of the upper mantle and the mantle wedge: A view from the experimentalists. In J. Eiler (Ed.), *Geophysical monograph series* (Vol. 138, pp. 83–105). American Geophysical Union. https://doi.org/10.1029/138GM06

Hirth, G., Teyssier, C., & Dunlap, J. W. (2001). An evaluation of quartzite flow laws based on comparisons between experimentally and naturally deformed rocks. *International Journal of Earth Sciences*, *90*(1), 77–87. https://doi.org/10.1007/s005310000152

Holland, T. J. B., & Powell, R. (2011). An improved and extended internally consistent thermodynamic dataset for phases of petrological interest, involving a new equation of state for solids: Thermodynamic dataset for phases of petrological interest. *Journal of Metamorphic Geology*, *29*(3), 333–383. https://doi.org/10.1111/j.1525-1314.2010.00923.x

Horning, G., Canales, J. P., Carbotte, S. M., Han, S., Carton, H., Nedimović, M. R., & van Keken, P. E. (2016). A 2-D tomographic model of the Juan de Fuca plate from accretion at axial seamount to subduction at the Cascadia margin from an active source ocean bottom seismometer survey. *Journal of Geophysical Research: Solid Earth*, *121*(8), 5859–5879. https://doi.org/10.1002/2016JB013228

Huber, K., Vrijmoed, J. C., & John, T. (2022). Formation of olivine veins by reactive fluid flow in a dehydrating serpentinite. *Geochemistry, Geophysics, Geosystems*, *23*(6), e2021GC010267. https://doi.org/10.1029/2021GC010267

Hyndman, R. D., McCrory, P. A., Wech, A., Kao, H., & Ague, J. (2015). Cascadia subducting plate fluids channelled to fore-arc mantle corner: ETS and silica deposition. *Journal of Geophysical Research: Solid Earth*, *120*(6), 4344–4358. https://doi.org/10.1002/2015JB011920

Hyndman, R. D., & Peacock, S. M. (2003). Serpentinization of the forearc mantle. *Earth and Planetary Science Letters*, *212*(3–4), 417–432. https://doi.org/10.1016/S0012-821X(03)00263-2

Ivandic, M., Grevemeyer, I., Bialas, J., & Petersen, C. J. (2010). Serpentinization in the trench-outer rise region offshore of Nicaragua: Constraints from seismic refraction and wide-angle data. *Geophysical Journal International*, *180*(3), 1253–1264. https://doi.org/10.1111/j.1365-246X.2009.04474.x

Iwamori, H. (1998). Transportation of H_2O and melting in subduction zones. *Earth and Planetary Science Letters*, *160*(1–2), 65–80. https://doi.org/10.1016/S0012-821X(98)00080-6

John, T., Gussone, N., Podladchikov, Y. Y., Bebout, G. E., Dohmen, R., Halama, R., et al. (2012). Volcanic arcs fed by rapid pulsed fluid flow through subducting slabs. *Nature Geoscience*, *5*(7), 489–492. https://doi.org/10.1038/ngeo1482

Katz, R. F., Knepley, M. G., Smith, B., Spiegelman, M., & Coon, E. T. (2007). Numerical simulation of geodynamic processes with the portable extensible toolkit for scientific computation. *Physics of the Earth and Planetary Interiors*, *163*(1–4), 52–68. https://doi.org/10.1016/j.pepi.2007.04.016

Kawano, S., Katayama, I., & Okazaki, K. (2011). Permeability anisotropy of serpentinite and fluid pathways in a subduction zone. *Geology*, *39*(10), 939–942. https://doi.org/10.1130/G32173.1

Kirby, S. H., Durham, W. B., & Stern, L. A. (1991). Mantle phase changes and deep-earthquake faulting in subducting lithosphere. *Science*, *252*(5003), 216–225. https://doi.org/10.1126/science.252.5003.216

Kirkpatrick, J. D., Fagereng, Å., & Shelly, D. R. (2021). Geological constraints on the mechanisms of slow earthquakes. *Nature Reviews Earth & Environment*, *2*(4), 285–301. https://doi.org/10.1038/s43017-021-00148-w

Klein, E., Vigny, C., Duputel, Z., Zigone, D., Rivera, L., Ruiz, S., & Potin, B. (2023). Return of the Atacama deep slow slip event: The 5-year recurrence confirmed by continuous GPS. *Physics of the Earth and Planetary Interiors*, *334*, 106970. https://doi.org/10.1016/j.pepi.2022.106970

Kodaira, S., Iidaka, T., Kato, A., Park, J.-O., Iwasaki, T., & Kaneda, Y. (2004). High pore fluid pressure may cause silent slip in the Nankai trough. *Science*, *304*(5675), 1295–1298. https://doi.org/10.1126/science.1096535

Lee, C., Cerpa, N. G., Han, D., & Wada, I. (2024). Modeling liquid transport in the Earth's mantle as two-phase flow: Effect of an enforced positive porosity on liquid flow and mass conservation. *Solid Earth*, *15*(1), 23–38. https://doi.org/10.5194/se-15-23-2024

Lee, C., & Kim, Y. (2023). Understanding subduction infancy to mature subduction in Southwest Japan via the self-consistent formation of a weak slab interface. *Scientific Reports*, *13*(1), 21425. https://doi.org/10.1038/s41598-023-48746-6

Lee, C., Seoung, D., & Cerpa, N. G. (2021). Effect of water solubilities on dehydration and hydration in subduction zones and water transport to the deep mantle: Implications for natural subduction zones. *Gondwana Research*, *89*, 287–305. https://doi.org/10.1016/j.gr.2020.10.012

Li, Z., Wiens, D. A., Shen, W., & Shillington, D. J. (2024). Along-strike variations of Alaska subduction zone structure and hydration determined from amphibious seismic data. *Journal of Geophysical Research: Solid Earth*, *129*(3), e2023JB027800. https://doi.org/10.1029/2023JB027800

Malvoisin, B., Podladchikov, Y. Y., & Vrijmoed, J. C. (2015). Coupling changes in densities and porosity to fluid pressure variations in reactive porous fluid flow: Local thermodynamic equilibrium. *Geochemistry, Geophysics, Geosystems*, *16*(12), 4362–4387. https://doi.org/10.1002/2015GC006019

Maurice, J., Bolfan-Casanova, N., Padrón-Navarta, J. A., Manthilake, G., Hammouda, T., Hénot, J. M., & Andrault, D. (2018). The stability of hydrous phases beyond antigorite breakdown for a magnetite-bearing natural serpentinite between 6.5 and 11 GPa. *Contributions to Mineralogy and Petrology*, *173*(10), 86. https://doi.org/10.1007/s00410-018-1507-9

McLellan, M., & Audet, P. (2020). Uncovering the physical controls of deep subduction zone slow slip using supervised classification of subducting plate features. *Geophysical Journal International*, ggaa285. https://doi.org/10.1093/gji/ggaa285

Miller, N. C., Lizarralde, D., Collins, J. A., Holbrook, W. S., & Van Avendonk, H. J. A. (2021). Limited mantle hydration by bending faults at the Middle America Trench. *Journal of Geophysical Research: Solid Earth*, *126*(1), e2020JB020982. https://doi.org/10.1029/2020JB020982

Morishige, M., & Van Keken, P. E. (2018). Fluid migration in a subducting viscoelastic slab. *Geochemistry, Geophysics, Geosystems*, *19*(2), 337–355. https://doi.org/10.1002/2017GC007236

Muñoz-Montecinos, J., Angiboust, S., Garcia-Casco, A., Glodny, J., & Bebout, G. (2021). Episodic hydrofracturing and large-scale flushing along deep subduction interfaces: Implications for fluid transfer and carbon recycling (Zagros Orogen, southeastern Iran). *Chemical Geology*, *571*, 120173. https://doi.org/10.1016/j.chemgeo.2021.120173

Muñoz-Montecinos, J., Angiboust, S., Minnaert, C., Ceccato, A., Morales, L., Gasc, J., & Behr, W. (2024). Fluid-driven shear instabilities in the subducted oceanic mantle at intermediate depths: Insights from western Alps meta-ophiolites. *Geochemistry, Geophysics, Geosystems*, *25*(8), e2024GC011581. https://doi.org/10.1029/2024GC011581

Muñoz-Montecinos, J., & Behr, W. M. (2023). Transient permeability of a deep-seated subduction interface shear zone. *Geophysical Research Letters*, *50*(20), e2023GL104244. https://doi.org/10.1029/2023GL104244

Naif, S., Key, K., Constable, S., & Evans, R. L. (2015). Water-rich bending faults at the Middle America Trench. *Geochemistry, Geophysics, Geosystems*, *16*(8), 2582–2597. https://doi.org/10.1002/2015GC005927

Nishiyama, T. (1989). Kinetics of hydrofracturing and metamorphic veining. *Geology*, *17*(12), 1068–1071. https://doi.org/10.1130/0091-7613(1989)017<1068:KOHAMV>2.3.CO;2

Obana, K., Fujie, G., Takahashi, T., Yamamoto, Y., Tonegawa, T., Miura, S., & Kodaira, S. (2019). Seismic velocity structure and its implications for oceanic mantle hydration in the trench–outer rise of the Japan Trench. *Geophysical Journal International*, *217*(3), 1629–1642. https://doi.org/10.1093/gji/ggz099

Obara, K. (2002). Nonvolcanic deep tremor associated with subduction in southwest Japan. *Science*, *296*(5573), 1679–1681. https://doi.org/10.1126/science.1070378

Ohta, Y., Freymueller, J., Hreinsdottir, S., & Suito, H. (2006). A large slow slip event and the depth of the seismogenic zone in the south central Alaska subduction zone. *Earth and Planetary Science Letters*, *247*(1–2), 108–116. https://doi.org/10.1016/j.epsl.2006.05.013

Okamoto, A., & Shimizu, H. (2015). Contrasting fracture patterns induced by volume-increasing and -decreasing reactions: Implications for the progress of metamorphic reactions. *Earth and Planetary Science Letters*, *417*, 9–18. https://doi.org/10.1016/j.epsl.2015.02.015

Okamoto, A., Shimizu, H., Fukuda, J., Muto, J., & Okudaira, T. (2017). Reaction-induced grain boundary cracking and anisotropic fluid flow during prograde devolatilization reactions within subduction zones. *Contributions to Mineralogy and Petrology*, *172*(9), 1–23. https://doi.org/10.1007/s00410-017-1393-6

Okamoto, K., & Maruyama, S. (1999). The high-pressure synthesis of lawsonite in the MORB+H_2O system. *American Mineralogist*, *84*(3), 362–373. https://doi.org/10.2138/am-1999-0320

Pawley, A. (2003). Chlorite stability in mantle peridotite: The reaction clinochlore+enstatite=forsterite+pyrope+H_2O. *Contributions to Mineralogy and Petrology*, *144*(4), 449–456. https://doi.org/10.1007/s00410-002-0409-y

Peacock, S. M., Christensen, N. I., Bostock, M. G., & Audet, P. (2011). High pore pressures and porosity at 35 km depth in the Cascadia subduction zone. *Geology*, *39*(5), 471–474. https://doi.org/10.1130/G31649.1

Piccoli, F., Ague, J. J., Chu, X., Tian, M., & Vitale Brovarone, A. (2021). Field-based evidence for intra-slab high-permeability channel formation at Eclogite-Facies conditions during subduction. *Geochemistry, Geophysics, Geosystems*, *22*(3), e2020GC009520. https://doi.org/10.1029/2020GC009520

Plümper, O., John, T., Podladchikov, Y. Y., Vrijmoed, J. C., & Scambelluri, M. (2017). Fluid escape from subduction zones controlled by channel-forming reactive porosity. *Nature Geoscience*, *10*(2), 150–156. https://doi.org/10.1038/ngeo2865

Ranero, C. R., Phipps Morgan, J., McIntosh, K., & Reichert, C. (2003). Bending-related faulting and mantle serpentinization at the Middle America trench. *Nature*, *425*(6956), 367–373. https://doi.org/10.1038/nature01961

Ranero, C. R., & Sallarès, V. (2004). Geophysical evidence for hydration of the crust and mantle of the Nazca plate during bending at the north Chile trench. *Geology*, *32*(7), 549. https://doi.org/10.1130/G20379.1

Ribe, N. M. (2010). Bending mechanics and mode selection in free subduction: A thin-sheet analysis. *Geophysical Journal International*, *180*(2), 559–576. https://doi.org/10.1111/j.1365-246X.2009.04460.x

Rogers, G., & Dragert, H. (2003). Episodic tremor and slip on the Cascadia subduction zone: The Chatter of silent slip. *Science*, *300*(5627), 1942–1943. https://doi.org/10.1126/science.1084783

Rolandone, F., Nocquet, J.-M., Mothes, P. A., Jarrin, P., Vallée, M., Cubas, N., et al. (2018). Areas prone to slow slip events impede earthquake rupture propagation and promote afterslip. *Science Advances*, *4*(1), eaao6596. https://doi.org/10.1126/sciadv.aao6596

Rose, I. R., & Korenaga, J. (2011). Mantle rheology and the scaling of bending dissipation in plate tectonics. *Journal of Geophysical Research*, *116*(B6), B06404. https://doi.org/10.1029/2010JB008004

Royer, A. A., Thomas, A. M., & Bostock, M. G. (2015). Tidal modulation and triggering of low-frequency earthquakes in northern Cascadia. *Journal of Geophysical Research: Solid Earth*, *120*(1), 384–405. https://doi.org/10.1002/2014JB011430

Rudge, J. F. (2018). Textural equilibrium melt geometries around tetrakaidecahedral grains. *Proceedings of the Royal Society A: Mathematical, Physical and Engineering Sciences*, *474*(2212), 20170639. https://doi.org/10.1098/rspa.2017.0639

Rupke, L. (2004). Serpentine and the subduction zone water cycle. *Earth and Planetary Science Letters*, *223*(1–2), 17–34. https://doi.org/10.1016/j.epsl.2004.04.018

Saffer, D. M., & Tobin, H. J. (2011). Hydrogeology and mechanics of subduction zone forearcs: Fluid flow and pore pressure. *Annual Review of Earth and Planetary Sciences*, *39*(1), 157–186. https://doi.org/10.1146/annurev-earth-040610-133408

Schellart, W. P. (2008). Kinematics and flow patterns in deep mantle and upper mantle subduction models: Influence of the mantle depth and slab to mantle viscosity ratio. *Geochemistry, Geophysics, Geosystems*, *9*(3), 2007GC001656. https://doi.org/10.1029/2007GC001656

Schmalholz, S. M., Moulas, E., Räss, L., & Müntener, O. (2023). Serpentinite dehydration and Olivine Vein formation during ductile shearing: Insights from 2D numerical modeling on porosity generation, density variations, and transient weakening. *Journal of Geophysical Research: Solid Earth*, *128*(11), e2023JB026985. https://doi.org/10.1029/2023JB026985

Schmidt, M. W., & Poli, S. (1998). Experimentally based water budgets for dehydrating slabs and consequences for arc magma generation. *Earth and Planetary Science Letters*, *163*(1–4), 361–379. https://doi.org/10.1016/S0012-821X(98)00142-3

Scott, D. R., & Stevenson, D. J. (1984). Magma solitons. *Geophysical Research Letters*, *11*(11), 1161–1164. https://doi.org/10.1029/GL011i011p01161

Spiegelman, M. (1993). Flow in deformable porous media. Part 1 Simple analysis. *Journal of Fluid Mechanics*, *247*, 17–38. https://doi.org/10.1017/S0022112093000369

Stein, C. A., & Stein, S. (1992). A model for the global variation in oceanic depth and heat flow with lithospheric age. *Nature*, *359*(6391), 123–129. https://doi.org/10.1038/359123a0

Syracuse, E. M., & Abers, G. A. (2006). Global compilation of variations in slab depth beneath arc volcanoes and implications. *Geochemistry, Geophysics, Geosystems*, *7*(5), 2005GC001045. https://doi.org/10.1029/2005GC001045

Taetz, S., John, T., Bröcker, M., Spandler, C., & Stracke, A. (2018). Fast intraslab fluid-flow events linked to pulses of high pore fluid pressure at the subducted plate interface. *Earth and Planetary Science Letters*, *482*, 33–43. https://doi.org/10.1016/j.epsl.2017.10.044

Tian, M., Katz, R. F., & Rees Jones, D. W. (2019). Devolatilization of subducting slabs, Part I: Thermodynamic parameterization and open system effects. *Geochemistry, Geophysics, Geosystems*, *20*(12), 5667–5690. https://doi.org/10.1029/2019GC008488

Tian, M., Katz, R. F., Rees Jones, D. W., & May, D. A. (2019). Devolatilization of subducting slabs, Part II: Volatile fluxes and storage. *Geochemistry, Geophysics, Geosystems*, *20*(12), 6199–6222. https://doi.org/10.1029/2019GC008489

Tibaldi, A. (1992). The role of transcurrent intra-arc tectonics in the configuration of a volcanic arc. *Terra Nova*, *4*(5), 567–577. https://doi.org/10.1111/j.1365-3121.1992.tb00598.x

Tielke, J. A., Zimmerman, M. E., & Kohlstedt, D. L. (2017). Hydrolytic weakening in olivine single crystals. *Journal of Geophysical Research: Solid Earth*, *122*(5), 3465–3479. https://doi.org/10.1002/2017JB014004

Tulley, C. J., Fagereng, Å., Ujiie, K., Diener, J. F. A., & Harris, C. (2022). Embrittlement within viscous shear zones across the base of the subduction thrust seismogenic zone. *Geochemistry, Geophysics, Geosystems*, *23*(9), e2021GC010208. https://doi.org/10.1029/2021GC010208

Ulmer, P., & Trommsdorff, V. (1995). Serpentine stability to mantle depths and subduction-related magmatism. *Science, New Series*, *268*(5212), 858–861. https://doi.org/10.1126/science.268.5212.858

Van Avendonk, H. J. A., Holbrook, W. S., Lizarralde, D., & Denyer, P. (2011). Structure and serpentinization of the subducting Cocos plate offshore Nicaragua and Costa Rica. *Geochemistry, Geophysics, Geosystems*, *12*(6), Q06009. https://doi.org/10.1029/2011GC003592

Van Keken, P. E., Hacker, B. R., Syracuse, E. M., & Abers, G. A. (2011). Subduction factory: 4. Depth-dependent flux of H_2O from subducting slabs worldwide. *Journal of Geophysical Research*, *116*(B1), B01401. https://doi.org/10.1029/2010JB007922

Van Keken, P. E., Kiefer, B., & Peacock, S. M. (2002). High-resolution models of subduction zones: Implications for mineral dehydration reactions and the transport of water into the deep mantle. *Geochemistry, Geophysics, Geosystems*, *3*(10), 1056. https://doi.org/10.1029/2001GC000256

Van Keken, P. E., Wada, I., Abers, G. A., Hacker, B. R., & Wang, K. (2018). Mafic high-pressure rocks are preferentially exhumed from warm subduction settings. *Geochemistry, Geophysics, Geosystems*, *19*(9), 2934–2961. https://doi.org/10.1029/2018GC007624

Von Bargen, N., & Waff, H. S. (1986). Permeabilities, interfacial areas and curvatures of partially molten systems: Results of numerical computations of equilibrium microstructures. *Journal of Geophysical Research*, *91*(B9), 9261–9276. https://doi.org/10.1029/JB091iB09p09261

Wada, I., Behn, M. D., & Shaw, A. M. (2012). Effects of heterogeneous hydration in the incoming plate, slab rehydration, and mantle wedge hydration on slab-derived H_2O flux in subduction zones. *Earth and Planetary Science Letters*, *353–354*, 60–71. https://doi.org/10.1016/j.epsl.2012.07.025

Wada, I., & Wang, K. (2009). Common depth of slab-mantle decoupling: Reconciling diversity and uniformity of subduction zones. *Geochemistry, Geophysics, Geosystems*, *10*(10), 2009GC002570. https://doi.org/10.1029/2009GC002570

Wada, I., Wang, K., He, J., & Hyndman, R. D. (2008). Weakening of the subduction interface and its effects on surface heat flow, slab dehydration, and mantle wedge serpentinization. *Journal of Geophysical Research*, *113*(B4), 2007JB005190. https://doi.org/10.1029/2007JB005190

Walowski, K. J., Wallace, P. J., Hauri, E. H., Wada, I., & Clynne, M. A. (2015). Slab melting beneath the Cascade Arc driven by dehydration of altered oceanic peridotite. *Nature Geoscience*, *8*(5), 404–408. https://doi.org/10.1038/ngeo2417

Wang, K., & Bilek, S. L. (2014). Invited review paper: Fault creep caused by subduction of rough seafloor relief. *Tectonophysics*, *610*, 1–24. https://doi.org/10.1016/j.tecto.2013.11.024

Wark, D. A., & Watson, E. B. (1998). Grain-scale permeabilities of texturally equilibrated, monomineralic rocks. *Earth and Planetary Science Letters*, *164*(3–4), 591–605. https://doi.org/10.1016/S0012-821X(98)00252-0

Wark, D. A., Williams, C. A., Watson, E. B., & Price, J. D. (2003). Reassessment of pore shapes in microstructurally equilibrated rocks, with implications for permeability of the upper mantle. *Journal of Geophysical Research*, *108*(B1), 2001JB001575. https://doi.org/10.1029/2001JB001575

Wilson, C. R., Spiegelman, M., & Van Keken, P. E. (2017). TerraFERMA: The transparent finite element rapid model assembler for multiphysics problems in Earth sciences. *Geochemistry, Geophysics, Geosystems*, *18*(2), 769–810. https://doi.org/10.1002/2016GC006702

Wilson, C. R., Spiegelman, M., Van Keken, P. E., & Hacker, B. R. (2014). Fluid flow in subduction zones: The role of solid rheology and compaction pressure. *Earth and Planetary Science Letters*, *401*, 261–274. https://doi.org/10.1016/j.epsl.2014.05.052

Xia, S., Zhao, D., & Qiu, X. (2008). Tomographic evidence for the subducting oceanic crust and forearc mantle serpentinization under Kyushu, Japan. *Tectonophysics*, *449*(1), 85–96. https://doi.org/10.1016/j.tecto.2007.12.007

Yamasaki, T., & Seno, T. (2003). Double seismic zone and dehydration embrittlement of the subducting slab. *Journal of Geophysical Research*, *108*(B4), 2212. https://doi.org/10.1029/2002JB001918

Zhang, J., & Green, H. W. (2007). Experimental investigation of eclogite rheology and its fabrics at high temperature and pressure. *Journal of Metamorphic Geology*, *25*(2), 97–115. https://doi.org/10.1111/j.1525-1314.2006.00684.x

Zhang, J., Zhang, F., Lin, J., Gao, X., Cai, C., & Zhou, Z. (2024). Mantle serpentinization of subducting plate are controlled by combined effect of plate age and bending curvature. *Earth and Planetary Science Letters*, *640*, 118799. https://doi.org/10.1016/j.epsl.2024.118799

Zhong, X., & Galvez, M. E. (2022). The subducting slab as a chromatographic column: Regimes of sub-solidus mass transport as a function of lithospheric hydration state, with special reference to the fate of carbonate. *Journal of Geophysical Research: Solid Earth*, *127*(6), e2021JB023851. https://doi.org/10.1029/2021JB023851